International Journal of Hydrogen Energy 240 (2026) 155391

Contents lists available at ScienceDirect

International Journal of Hydrogen Energy

journal homepage: www.elsevier.com/locate/he

Grid-integrated hydrogen production systems: A holistic analytical modeling framework for stability assessment and dynamic interaction

Chunjun Huang [a], José Luis Rueda Torres [a,*], Nakul Narayanan Kuruveettil [b], Xin Jin [c,*]

[a] Department of Electrical Sustainable Energy, Delft University of Technology, Delft, 2628 CD, The Netherlands
[b] Department of Electrical Engineering, Government Engineering College, Thrissur, India
[c] Department of Energy and Process Engineering, Norwegian University of Science and Technology, Trondheim NO 7491, Norway

ARTICLE INFO

Keywords:
Hydrogen production
PEM electrolyzer
Analytical model
Stability assessment
Grid-interaction analysis

ABSTRACT

Grid-integrated electrolyzer systems are increasingly deployed for green hydrogen production, which is a promising pathway for energy decarbonization. However, their operation is challenged by insufficiently understood dynamic interactions among the grid-side rectifier, the buck converter, their control loops, and the electrolyzer stack. To address this issue, this paper develops a holistic analytical framework for such systems. A unified model is derived by integrating the rectifier, the buck converter, their control loops, and the electrolyzer stack. Based on this model, eigenvalue, participation-factor, and frequency-response analyses are conducted to systematically quantify stability characteristics, internal dynamic couplings, and parameter sensitivities. For a 2 MW electrolyzer case, the results reveal that excessive rectifier or buck-control bandwidths can independently trigger distinct oscillatory instabilities. On this basis, engineering-oriented controller-tuning guidelines are established, recommending about 10–50 Hz for the phase-locked loop, below about 60 Hz for the DC-link voltage controller, and about 20–150 Hz for the buck power controller. The analysis further shows that properly designed buck bandwidth renders the system-level power response weakly sensitive to slow electrolyzer dynamics dominated by double-layer capacitance, thereby mitigating uncertainty in this capacitance and clarifying the applicability of reduced-order electrolyzer models. These findings are corroborated by PSCAD/EMTDC time-domain simulations, verifying the effectiveness of the proposed analytical model. Additional verifications under frequency and voltage disturbances further confirm the model's predictive capability, with maximum relative errors of 0.264%–1.486% and 0.153%–5.922%, respectively. Overall, this work offers an efficient analytical tool for stability-oriented control design, model-fidelity selection, and dynamic interaction analysis of grid-integrated electrolyzer systems.

1. Introduction

The accelerating transition toward low-carbon energy systems has led to the widespread deployment of variable renewable energy sources. As their increasing penetration introduces pronounced intermittency and uncertainty, advanced energy storage and conversion technologies have become essential to maintain operational reliability and stability of energy systems. In this context, green hydrogen produced via renewable-powered water electrolysis has gained considerable attention, offering both long-term energy storage capability and a viable pathway for decarbonizing hard-to-electrify industrial processes [1]. Among the available electrolysis technologies, proton exchange membrane (PEM) electrolyzers are particularly attractive for grid-interactive applications where flexible and dynamically varying operation is often required, owing to their fast dynamic response, high power density, and wide operating range [2–4]. Recent studies have further shown that PEM electrolyzers are well suited for flexible and transient operation under intermittent power input from renewable sources, while renewable-coupled operation may also induce non-negligible system-level dynamic effects, including efficiency variations, temperature and pressure deviations [3,5]. PEM electrolyzers are commonly interfaced with the power grid through cascaded power electronic converters, forming tightly coupled multi-domain systems that integrate electrical, control, and electrochemical subsystems [6,7]. The tight interactions among these subsystems give rise to complex dynamic characteristics and cross-coupled control behaviors that can significantly influence overall system stability and remain insufficiently characterized.

Recent PEM electrolyzer studies have also made progress in dynamic modeling from complementary perspectives. In particular, control-oriented and stack-side dynamic models have been developed

* Corresponding authors.
E-mail addresses: jruedatorres@tudelft.nl (J.L.R. Torres), xin.jin1@ntnu.no (X. Jin).

https://doi.org/10.1016/j.ijhydene.2026.155391
Received 12 February 2026; Received in revised form 29 April 2026; Accepted 3 May 2026
Available online 12 May 2026

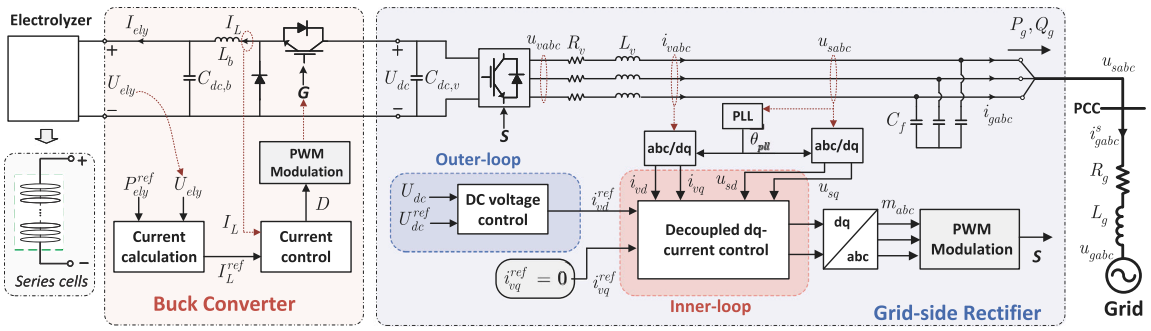

Fig. 1. Circuit and control structure of the grid-integrated electrolyzer system.

to better capture transient electrochemical behavior and double-layer-capacitance-related effects [4,8], while system-level dynamic models have been reported to represent the overall behavior of PEM electrolyzer systems including key auxiliary units [9]. These studies provide valuable recent background for PEM-electrolyzer modeling. However, they mainly focus on stack-side dynamics or plant-level operational behavior, overlooking the holistic interaction among grid-side converters, multiple control loops, and the PEM stack in grid-integrated applications.

Meanwhile, research has increasingly explored electrolyzers as active controllable loads capable of providing ancillary services, including fast frequency support [10,11], synthetic inertia [12], renewable power smoothing [13,14], and market participation [15,16]. Achieving these demanding grid-support functions relies on high-bandwidth control to ensure fast power regulation, yet such control pushes the system close to its stability limits. Thus, small-signal stability analysis is essential to ensure reliable operation of electrolyzer systems, considering the complex dynamic interactions among internal components and control loops. Two principal analytical frameworks exist: state-space model-driven eigenvalue analysis and impedance-based analysis. The eigenvalue analysis method provides deep design insights by capturing couplings among all physical and control states, making it ideal for identifying root causes of instability and guiding parameter tuning [17,18]. The impedance-based analysis method enables terminal stability assessment without internal model knowledge [19,20].

Recent studies have begun applying these stability analysis methods to evaluate the stability of grid-integrated electrolyzers. For instance, impedance-based methods are used in [21] to analyze a thyristor-rectifier-fed electrolyzer system, and in [22] to study power tracking in a co-located wind-hydrogen plant. The latter also proposes an optimal partitioning method for implementing impedance calculation to handle cross-plant feedback loops. However, both studies focus on thyristor-based converters, whose dynamics and resulting stability properties are fundamentally different from fully controllable converters. Since grid-support applications require fast and flexible power regulation, fully controllable converter architectures are more suitable, yet their stability characteristics remain insufficiently explored. To address this gap, a more recent study [23] uses a state-space approach to examine the small-signal stability of an electrolyzer system with a two-stage active-front-end plus DC–DC (AFE+DC) converter. This converter is attracting growing attention because it offers grid-friendly behavior and provides the voltage and current matching required by high-power electrolyzers [24–26]. While the study [23] explores the impact of physical parameters such as operating point, DC-link capacitance, and grid strength, its model does not holistically integrate the dynamics of the converter's multiple control loops for providing fast power regulation. As a result, it does not reveal the dynamic coupling between the converters and the electrolyzer or the influence of control-parameter design on system stability boundaries.

Accordingly, the existing literature reveals a key research gap: the absence of a holistic analytical modeling approach capable of quantifying the internal dynamic couplings and small-signal stability limits of grid-integrated electrolyzer systems using an AFE+DC-based controllable converter. Such an analytical modeling is essential for understanding the interactions between the electrolyzer's electrochemical dynamics and the converter's multiple control loops. It is also crucial for assessing the sensitivity of system stability to control parameters, particularly under fast power-regulation requirements for grid-support applications.

To overcome the above limitations, this paper proposes a holistic analytical modeling framework for AFE+DC-based grid-integrated electrolyzer systems, providing an efficient theoretical tool for quantitatively characterizing internal dynamic interactions and performing stability assessment. The main contributions of this work can be summarized as follows:

(1) A unified state-space model is developed, which fully integrates the dynamics of the grid-side AFE rectifier, the DC–DC converter, their associated control loops, and the PEM electrolyzer stack.

(2) The impact of key control parameters on system stability is quantitatively characterized through eigenvalue-based analysis, revealing the underlying interaction mechanisms that link controller bandwidth design to system-level dynamic performance and stability limits.

(3) A principle for electrolyzer model order reduction is established, demonstrating that by strategically designing the DC–DC controller bandwidth, the system-level power response becomes weakly sensitive to the PEM stack's double-layer-capacitance-dominated internal dynamics. This provides a theoretical basis for utilizing simplified stack models in system-level studies.

The remainder of this paper is organized as follows: Section 2 details the system configuration and derives the comprehensive analytical model. Section 3 presents the system's small-signal stability analysis based on the proposed model. Section 4 provides the time-domain demonstration of the analytical findings against detailed electromagnetic transient (EMT) simulations. Finally, Section 5 summarizes the main conclusions and outlines future work.

2. Proposed analytical modeling of the grid-integrated electrolyzer system

2.1. System description

The configuration of the grid-integrated electrolyzer system under study is depicted in Fig. 1. The system employs a two-stage power conversion architecture (i.e., AFE+DC) to interface a PEM electrolyzer stack with the AC grid, comprising a grid-side rectifier and a DC–DC buck converter. The first stage, a three-phase AFE converter acting as the grid-side rectifier, connects to the grid at the point of common coupling (PCC). Its primary control objectives are to maintain a stable DC-link voltage and regulate the reactive power, typically to ensure unity power factor operation by maintaining a zero reactive current reference. This is achieved using a cascaded vector control strategy implemented in the synchronous reference frame (dq-frame),

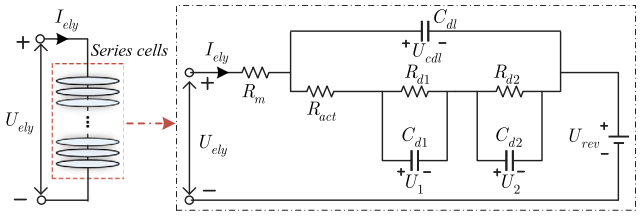

Fig. 2. Equivalent electrical circuit model of the PEM electrolyzer stack.

synchronized with the grid voltage via a phase-locked loop (PLL). The subsequent buck converter stage steps down the high DC-link voltage to a lower voltage level needed for the stack and regulates the stack power consumption through a dedicated power controller. The external AC grid is represented by its Thevenin equivalent with a series grid impedance comprising a resistor (R_g) and an inductor (L_g).

As illustrated, the overall system constitutes a tightly coupled entity where the dynamics of multiple physical subsystems, including the electrolyzer stack, buck converter, DC link, grid-side rectifier, and AC grid interface, are intricately linked with the behavior of multiple controllers. The dynamic behavior is thus governed by the complex interplay between these physical components and multiple control parameters distributed across different timescales. A comprehensive analytical model is therefore critical to quantitatively reveal these dynamics, understand the underlying influence of key parameters, and to analyze the stability impacts of such interactions. Accordingly, the following subsections systematically develop this analytical model by first establishing the mathematical representation for each key subsystem and then integrating them into a holistic state-space framework for the entire system.

2.2. Modeling of the PEM electrolyzer stack

For grid-interaction studies, equivalent electrical circuit methods are widely adopted for modeling PEM electrolyzers, as they capture the key electrochemical dynamics with a favorable balance of fidelity and complexity [27,28]. This study employs the well-established equivalent electrical circuit model for a single PEM cell from [28]. The complete stack model is then developed by assuming identical cells are connected in series. The topology of this circuit model, depicted in Fig. 2, utilizes several resistive–capacitive branches to emulate the dynamic behavior of the various overpotentials within the stack.

Based on this circuit topology, the dynamic behavior of the electrolyzer stack is mathematically formulated by the following state-space representation:

$$\dot{\mathbf{x}}_\mathbf{e} = \mathbf{A}_\mathbf{e}\,\mathbf{x}_\mathbf{e} + \mathbf{B}_\mathbf{e}\,\mathbf{u}_\mathbf{e} \tag{1a}$$

$$\mathbf{y}_\mathbf{e} = \mathbf{C}_\mathbf{e}\,\mathbf{x}_\mathbf{e} + \mathbf{D}_\mathbf{e}\,\mathbf{u}_\mathbf{e} - \frac{U_{rev}}{R_m} \tag{1b}$$

$$\mathbf{x}_\mathbf{e} = \begin{bmatrix} U_{cdl} & U_1 & U_2 \end{bmatrix}^\mathsf{T},\ \mathbf{u}_\mathbf{e} = U_{ely},\ \mathbf{y}_\mathbf{e} = I_{ely} \tag{1c}$$

where U_{cdl}, U_1, U_2 are the voltage at capacitors C_{dl}, C_{d1}, C_{d2}, respectively; U_{rev} denotes the equivalent reversible voltage of the entire stack, which is considered constant. The four coefficient matrices are:

$$\mathbf{A}_\mathbf{e} = \begin{bmatrix} -\frac{R_{act}+R_m}{C_{dl}R_{act}R_m} & \frac{1}{C_{dl}R_{act}} & \frac{1}{C_{dl}R_{act}} \\ \frac{1}{C_{d1}R_{act}} & -\frac{R_{d1}+R_{act}}{C_{d1}R_{d1}R_{act}} & -\frac{1}{C_{d1}R_{act}} \\ \frac{1}{C_{d2}R_{act}} & -\frac{1}{C_{d2}R_{act}} & -\frac{R_{d2}+R_{act}}{C_{d2}R_{d2}R_{act}} \end{bmatrix} \tag{2a}$$

$$\mathbf{B}_\mathbf{e} = \begin{bmatrix} \frac{1}{R_m C_{dl}} & 0 & 0 \end{bmatrix}^\mathsf{T},\ \mathbf{C}_\mathbf{e} = \begin{bmatrix} -\frac{1}{R_m} & 0 & 0 \end{bmatrix},\ \mathbf{D}_\mathbf{e} = \frac{1}{R_m} \tag{2b}$$

where all R_i, C_i are the estimated model parameters that can be fitted via experimental testing for electrolyzers [28].

To provide an intuitive understanding of the internal dynamics, the state-space model is visualized as the signal-flow block diagram shown in Fig. 3. This diagram explicitly illustrates the causal chain through which an input supplied voltage U_{ely} propagates through the model. It shows how the internal state variables (U_{cdl}, U_1, U_2) evolve dynamically to collectively determine the final stack current I_{ely} as the output. By decomposing the mathematical model into its fundamental blocks, this graphical representation provides an intuitive view of the plant model, clarifying how the internal dynamics contribute to the overall U-I behavior of the electrolyzer stack. Note that the annotations (e.g., red/blue arrows) are consistently used in all subsequent modeling diagrams and will not be explained again for brevity.

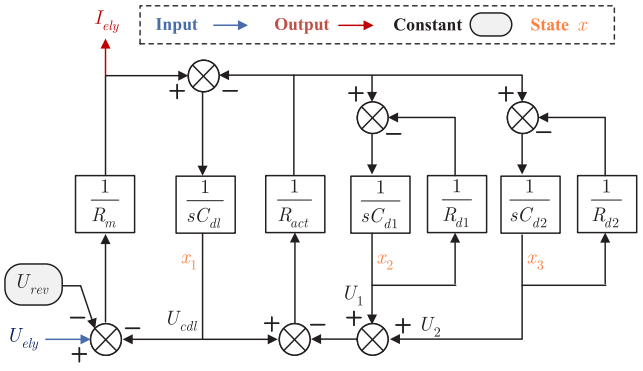

Fig. 3. Signal-flow block diagram of the PEM stack model.

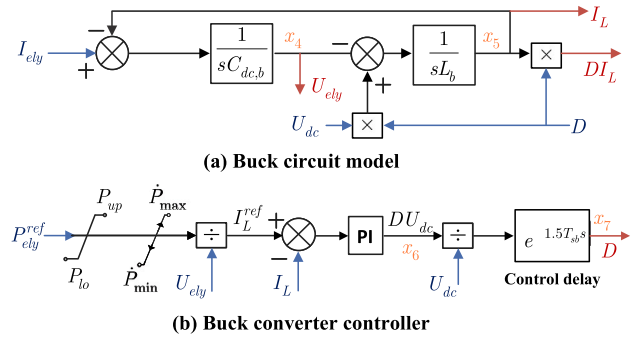

Fig. 4. Signal-flow block diagram of the buck converter model.

2.3. Modeling of the buck converter

The buck converter model is established using the well-known state-space averaging technique [29]. By selecting the inductor current I_L and the capacitor voltage U_{ely} as the state variables, and based on the buck circuit shown in Fig. 1, its dynamic model can be expressed as:

$$L_b \frac{dI_L}{dt} = DU_{dc} - U_{ely} \tag{3a}$$

$$C_{dc,b} \frac{dU_{ely}}{dt} = I_L - I_{ely} \tag{3b}$$

where L_b and $C_{dc,b}$ denote the inductance and capacitance of the buck converter, respectively; D represents the duty cycle of the controllable power semiconductor switch.

Accordingly, the signal-flow block diagram of the buck circuit model is established, as shown in Fig. 4(a), with multiple input and output ports to interface with other subsystem models. For example, the electrolyzer model provides the input current I_{ely}, while the duty ratio D is generated by the buck converter controller. The detailed structure of the proposed power controller is illustrated in Fig. 4(b).

In the proposed power control, a given power reference P_{ely}^{ref} is first processed by a magnitude limiter $[P_{lo}, P_{up}]$ and a ramp-rate limiter $[\dot{P}_{min}, \dot{P}_{max}]$ to ensure safe operation under electrolyzer's physical

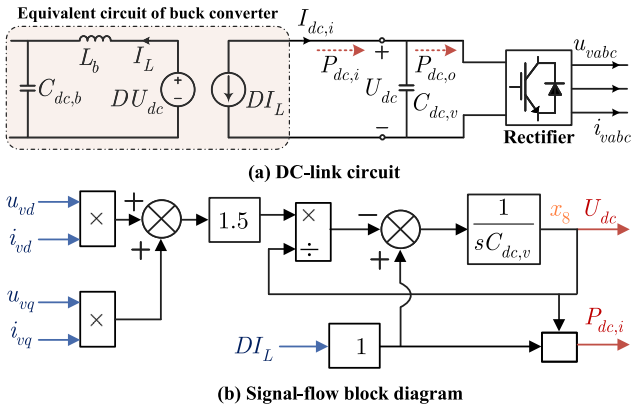

Fig. 5. Circuit topology and signal-flow block diagram of the DC-link model.

constraints, and then divided by the electrolyzer voltage to obtain the current reference I_L^{ref}. This reference is tracked by a proportional–integral (PI) current controller, which produces the regulation term DU_{dc}; after normalization by the input voltage U_{dc}, the ideal duty cycle is obtained. In practical digital control implementations, control delays are inevitable. To account for this, a control delay represented by $e^{-1.5T_{sb}s}$ (where T_{sb} is the reciprocal of the buck converter's switching frequency f_{sb}) is introduced, yielding the final duty ratio D, which is then modulated via PWM to generate the switching signals. This proposed controller straightforwardly enables a rapid power regulation by adjusting the input power reference. It ensures that the electrolyzer can execute fast-varying grid-support commands, such as those required for frequency regulation, while also supporting flexible partial-load operation of the electrolyzer itself.

2.4. Modeling of the grid-side rectifier

The grid-side AFE rectifier is directly connected to the buck converter through the DC-link, as shown in Fig. 5(a), which highlights the electrical interactions within the circuit. Based on the circuit topology, and applying the state-space averaging model to the buck converter, the DC-link dynamics can be described by (4). From this formulation, the corresponding signal-flow block diagram of the DC-link model is constructed, as shown in Fig. 5(b).

$$C_{dc}\frac{dU_{dc}}{dt} = \frac{P_{dc,i} - P_{dc,o}}{U_{dc}} \tag{4a}$$

$$P_{dc,i} = I_{dc,i}U_{dc} = -DI_L U_{dc} \tag{4b}$$

$$P_{dc,o} = 1.5 \cdot (u_{vd}i_{vd} + u_{vq}i_{vq}) \tag{4c}$$

Furthermore, based on the rectifier circuit shown in Fig. 1, the dq-domain AC-side dynamics can be obtained by aligning the d-axis with the PCC voltage u_{sabc}. The corresponding dynamic equations are expressed as:

$$L_v\frac{di_{vd}}{dt} + R_v i_{vd} = u_{vd} - u_{sd} + \omega_{pll}L_v i_{vq} \tag{5a}$$

$$L_v\frac{di_{vq}}{dt} + R_v i_{vq} = u_{vq} - u_{sq} - \omega_{pll}L_v i_{vd} \tag{5b}$$

$$C_f\frac{du_{sd}}{dt} = i_{vd} - i_{gd} + \omega_{pll}C_f u_{sq} \tag{5c}$$

$$C_f\frac{du_{sq}}{dt} = i_{vq} - i_{gq} - \omega_{pll}C_f u_{sd} \tag{5d}$$

where the subscripts d, q denote the respective dq-axis components of the three-phase variables $u_{vabc}, u_{sabc}, i_{vabc}, i_{gabc}$ (marked in Fig. 1); ω_{pll} is the fundamental angular frequency obtained from a PLL; L_v, R_v, and C_f are the inductance, resistance, and capacitance of the rectifier filter, respectively.

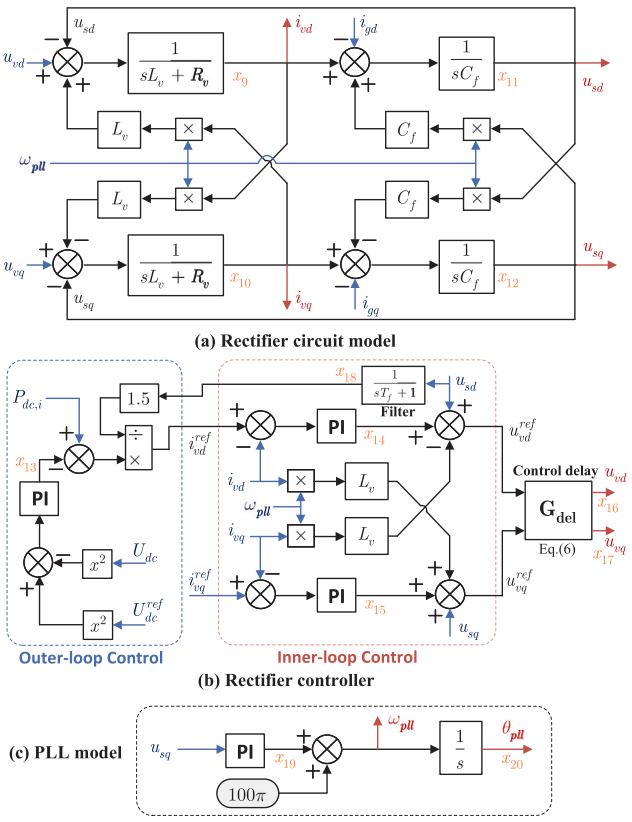

Fig. 6. Signal-flow block diagram of the rectifier model.

According to the dynamic equations, the signal-flow block diagram of the rectifier circuit model is built, as shown in Fig. 6(a). Two of the input signals, i.e., the rectifier voltages u_{vd} and u_{vq}, are generated by the rectifier controller. The controller structure is illustrated in Fig. 6(b), which is implemented in a synchronized dq-frame using a PLL to ensure synchronization. The PLL structure is shown in Fig. 6(c). The controller utilizes a widely-used cascaded control structure [29]. In the outer loop, a DC-link energy control (DLEC) is employed instead of DC-link voltage control to ensure a linear control system [30]. In this scheme, the error between the squared DC-link voltage and its squared reference is processed by a PI regulator, whose output is subsequently converted into the d-axis current reference i_{vd}^{ref}, while the q-axis current reference i_{vq}^{ref} is provided as an external input. The inner loop implements decoupled dq-current control, generating the rectifier voltage references u_{vd}^{ref} and u_{vq}^{ref}, which are then modulated via PWM to obtain the actual rectifier voltages u_{vd} and u_{vq}. Importantly, the effect of control delay inherent in digital implementation is also considered. The modulation delay in the dq-domain can be expressed as [31]:

$$\mathbf{G_{del}} = e^{-1.5T_{sv}s}\begin{bmatrix}\cos(1.5T_{sv}\omega_{pll}) & \sin(1.5T_{sv}\omega_{pll})\\ -\sin(1.5T_{sv}\omega_{pll}) & \cos(1.5T_{sv}\omega_{pll})\end{bmatrix} \tag{6}$$

where $T_{sv} = \frac{1}{f_{sv}}$, with f_{sv} denoting the rectifier switching frequency in Hz.

2.5. Modeling of the grid-side circuit

The grid-connection circuit topology of the electrolyzer system is shown in Fig. 7(a). Based on this configuration, the vector relationship between the PCC voltage and the grid voltage can be illustrated, as shown in Fig. 1(b). From the circuit topology and this vector relationship, the time-domain dynamics of the grid-side current in the synchronous reference frame can be derived, as given in (7). On this

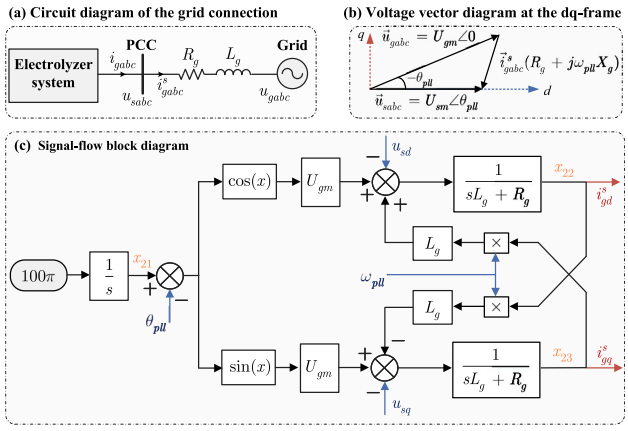

Fig. 7. Signal-flow block diagram of the grid-side circuit model.

basis, the corresponding signal-flow block diagram of the grid-side circuit model is constructed, as shown in Fig. 7(c).

$$L_g \frac{di^s_{gd}}{dt} + R_g i^s_{gd} = U_{gm}\cos(\omega_n t - \theta_{pll}) - u_{sd} + \omega_{pll} L_g i^s_{gq} \tag{7a}$$

$$L_g \frac{di^s_{gq}}{dt} + R_g i^s_{gq} = U_{gm}\sin(\omega_n t - \theta_{pll}) - u_{sq} - \omega_{pll} L_g i^s_{gd} \tag{7b}$$

where the subscripts d, q represent the dq-axis components of the three-phase variables u_{sabc}, u_{gabc}, and i^s_{gabc}; ω_n is the fundamental grid angular frequency (i.e., 100π rad/s).

2.6. Complete analytical model of entire system

By combining the previously established subsystem models, the complete analytical model of the entire grid-integrated electrolyzer system can be derived. Fig. 8 presents the schematic diagram of this analytical model, explicitly illustrating the interconnections among the subsystem models. To further support system scalability, the proposed model is formulated to remain applicable to large-scale electrolyzer systems. Such large-scale systems (e.g., at the hundreds of MW level), as shown in Fig. 9, typically consist of multiple electrolyzer units connected in parallel at the PCC. Moreover, at the unit level, each electrolyzer can also be scaled by combining several modules (including the stack and associated buck converter) in parallel via DC-coupled solutions [10,24].

These scalability characteristics can be explicitly reflected in the analytical model by linking the aggregate system currents to the number of modules and units. To this end, two scale factors, N_{mo} and N_{unit}, are introduced into the analytical model. A basic assumption is homogeneity across modules and units, i.e., neglecting parameter variations between them. This assumption is acceptable for system-level dynamic studies of electrolyzer systems, providing a reasonable trade-off between model fidelity and complexity. Based on this assumption and the system topology in Fig. 9, the total DC current ($I_{dc,i}$) from the buck converter to the DC-link, and the summed grid-side current (i^s_{gabc}) can be expressed as:

$$I_{dc,i} = -N_{mo} D I_L \tag{8a}$$

$$i^s_{gabc} = N_{unit} i_{gabc} \tag{8b}$$

where N_{mo} and N_{unit} are the number of modules and units, respectively; I_L is the inductor current of each buck converter; and i_{gabc} is the current through each electrolyzer unit.

Although the scalability formulation in (8) is established under the simplifying assumption of homogeneous modules and units, the impact of practical module-to-module parameter mismatch is further examined in Section 4.5 through an auxiliary heterogeneous-case study.

3. Small-signal stability and parametric dependency analysis

Based on the analytical model developed, the complete electrolyzer system can be expressed in a state-space form:

$$\dot{\mathbf{x}} = \mathbf{A}_{23\times23}(\mathbf{x},\mathbf{u}) \cdot \mathbf{x} + \mathbf{B}_{23\times3}(\mathbf{x},\mathbf{u}) \cdot \mathbf{u}, \tag{9a}$$

$$\mathbf{x} = \left[x_1, \cdots, x_{23}\right]^{\mathsf{T}}, \tag{9b}$$

$$\mathbf{u} = \left[P^{ref}_{ely}, U^{ref}_{dc}, i^{ref}_{vq}\right]^{\mathsf{T}}, \tag{9c}$$

where $\mathbf{x}$ denotes the 23-dimensional state vector with each state annotated in Fig. 3–Fig. 7, and $\mathbf{u}$ is the input vector consisting of the electrolyzer power reference, dc-link voltage reference, and q-axis current reference.

The state matrix $\mathbf{A}_{23\times23}(\mathbf{x},\mathbf{u})$ is not constant; it contains terms that depend on the system states and inputs, making the model in (9) inherently nonlinear. For small-signal stability assessment, the model is linearized by introducing perturbations around a nominal operating point [32]. This yields the linearized state matrix $\tilde{\mathbf{A}}$, obtained as the Jacobian of $\mathbf{A}(\mathbf{x},\mathbf{u})$ with respect to the states at the operating point. The system stability can then be analyzed using well-known linear analysis techniques, such as eigenvalue analysis of $\tilde{\mathbf{A}}$. It should be emphasized that the resulting eigenvalue-based conclusions are intended for local small-signal stability assessment around the nominal operating point, rather than for defining exact stability boundaries under arbitrary severe large-signal disturbances.

Therefore, based on the linearized system model, this section investigates the influence of key system parameters on small-signal stability. While physical parameters such as operating point, DC-link capacitance, and grid strength are known to be influential, their impact has been explored in recent work [23]. However, that study did not holistically integrate the dynamics of the converter's multiple control loops. Thus, it does not explicitly reveal the critical impact of control parameter design on the system's dynamics and stability boundaries. This study, therefore, concentrates on two critical areas not previously explored in detail for this system: the impact of converter control parameters and the electrolyzer stack's core dynamics. Specifically,

- **(1) Control Parameters:** The analysis focuses on the control bandwidth of each converter's loops (PLL, DLEC, and buck power control). Bandwidth is selected as the primary parameter because it directly dictates the system's response speed, which is a crucial factor for grid-support applications. However, an overly aggressive (high-bandwidth) control can compromise stability margins. This analysis is essential for guiding controller tuning for an electrolyzer system.
- **(2) Physical Parameters:** The analysis investigates the impact of the double-layer capacitance, C_{dl}, on both system stability and dynamic characteristics. This parameter represents the dominant dynamic of the electrolyzer stack and is a key source of model uncertainty, since it is generally not provided by manufacturers and is often estimated from rarely available dynamic test data using equivalent RC models [27]. Therefore, investigating the influence of this uncertain parameter is crucial for understanding how the electrolyzer stack's dynamics affects overall system stability and for determining the necessary model fidelity for grid-interaction studies.

The electrolyzer system parameters used for stability analysis are summarized in the Appendix (Table A.1). Unless otherwise stated, all remaining parameters retain the values listed in the table when evaluating the effect of an individual parameter.

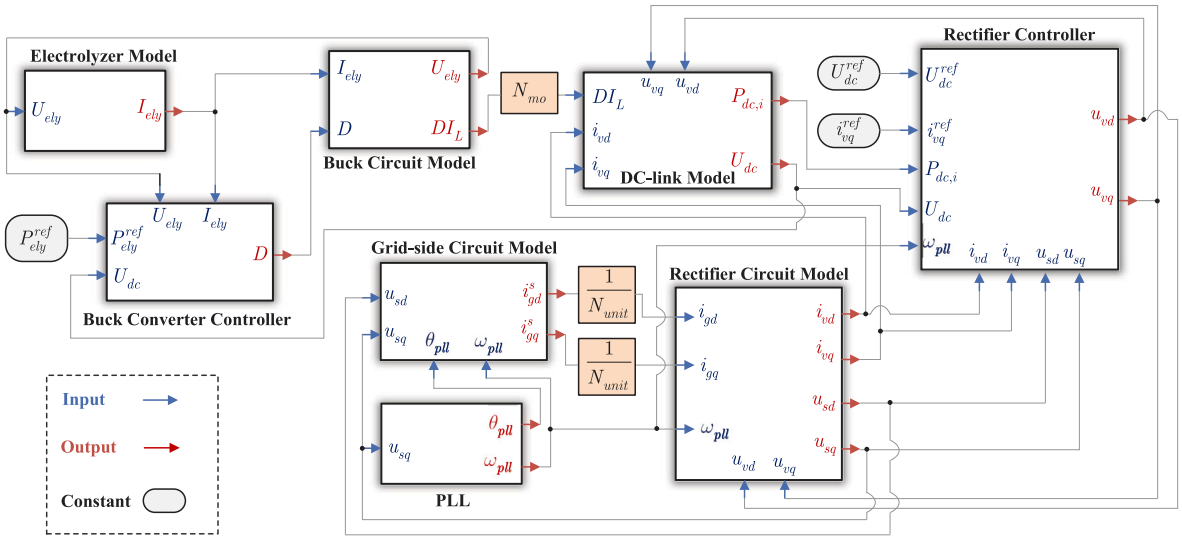

Fig. 8. Schematic diagram of the analytical model for the grid-integrated electrolyzer system (the subsystem models are shown in Fig. 3–Fig. 7).

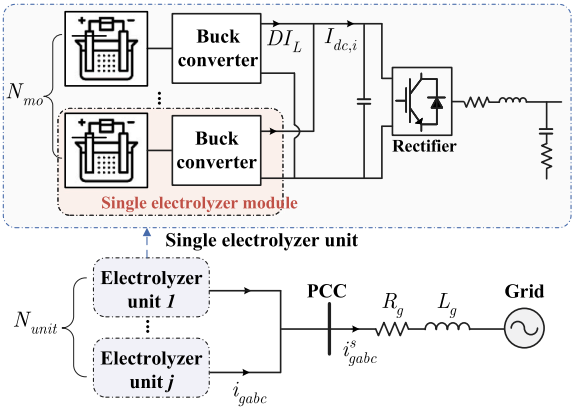

Fig. 9. Schematic diagram of a large-scale electrolyzer system integrating multiple DC-coupled modules and multiple parallel units at the PCC.

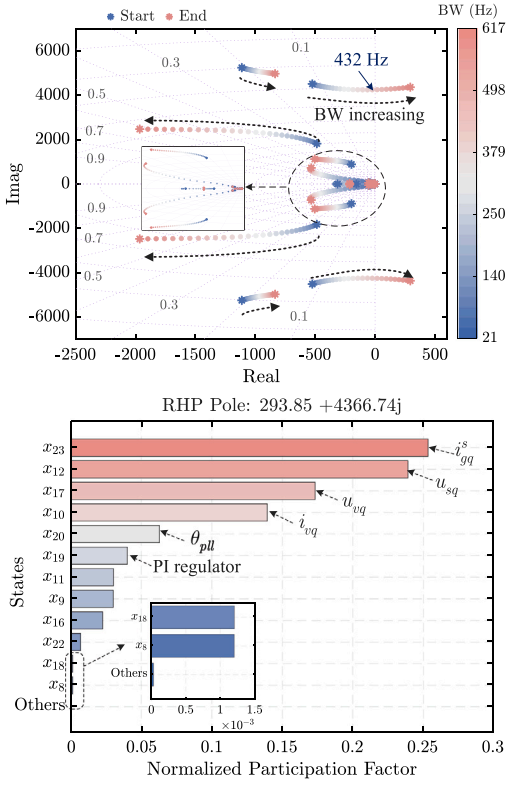

Fig. 10. Impact of the PLL bandwidth.

3.1. Impact of PLL bandwidth

The PLL dynamics described in Fig. 6(c) are governed by the transfer function:

$$G_{pll}(s) = \frac{U_{sm}k_p s + k_i U_{sm}}{s^2 + U_{sm}k_p s + k_i U_{sm}} \tag{10a}$$

$$k_{p,pll} = \frac{2\zeta_{pll}\omega_{n,pll}}{U_{sm}},\ k_{i,pll} = \frac{k_{p,pll}\omega_{n,pll}}{2\zeta_{pll}} \tag{10b}$$

where $\omega_{n,pll}$ and ζ_{pll} denote the natural frequency and damping ratio of the PLL, respectively; U_{sm} is the magnitude of PCC voltage $\vec{u}_{sabc}$; $k_{p,pll}$, $k_{i,pll}$ are the proportional and integral gains of the PI controller, respectively.

According to (10), the PLL exhibits a second-order system with a zero. The damping ratio ζ_{pll} is set to 0.707, which is a commonly used optimal value for second-order systems. With a fixed damping ratio, the PI controller gains are determined solely by the natural frequency $\omega_{n,pll}$. Due to the presence of a zero in (10), the true closed-loop bandwidth $\omega_{bw,pll}$, is proportional to $\omega_{n,pll}$, satisfying: $\omega_{bw,pll} \approx 2.058 \cdot \omega_{n,pll}$ for $\zeta_{pll} = 0.707$. As the sole tuning parameter, the bandwidth $\omega_{bw,pll}$ directly governs the PLL's response speed and its impact on system stability.

Accordingly, the impact of $\omega_{bw,pll}$ on system stability is evaluated. The results in Fig. 10 indicate that increasing the PLL bandwidth $\omega_{bw,pll}$ significantly affects the system stability. As the bandwidth increases from 21 Hz to 617 Hz, with the damping ratio $\zeta_{pll} = 0.707$, the dominant poles move towards the right-half plane (RHP), leading to unstable oscillatory modes around 690 Hz. The root locus clearly shows that a higher PLL bandwidth enhances the system's dynamic response but simultaneously reduces stability margins. The participation factor analysis (the bottom plot in Fig. 10) under an unstable RHP pole $293.85 + j4366.74$ further reveals that: the unstable mode is dominated by states associated with the q-axis components of the system's states, including i^s_{gq}, u_{sq}, u_{vq}, i_{vq}. This is because the q-axis PCC voltage u_{sq} is the input for the PLL. Besides, the PLL's own states, including its output

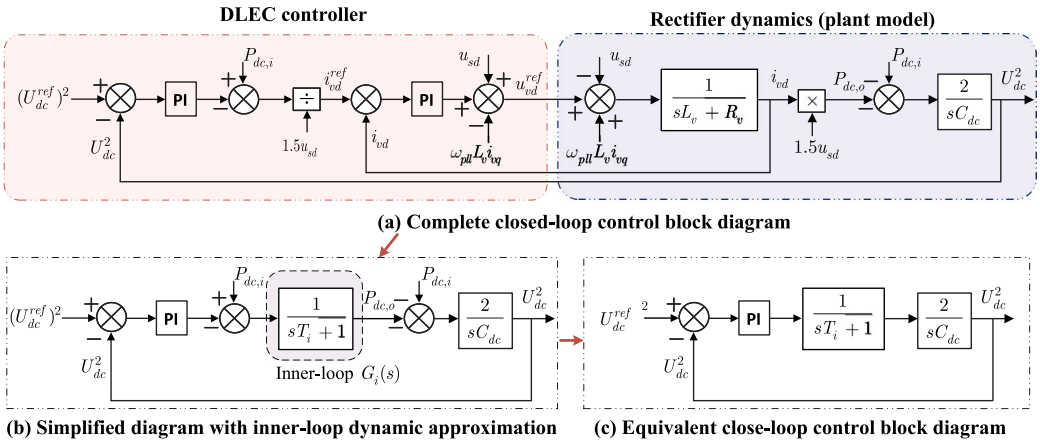

Fig. 11. Closed-loop control block diagram of the DLEC method for the rectifier.

phase angle θ_{pll} and the state of its PI controller, also show high participation. These results imply that over-aggressive PLL tuning intensifies the coupling between the PLL dynamics and the q-axis current loop, which ultimately drives the RHP pole migration and destabilizes the system. Therefore, the PLL bandwidth should be strategically designed to strike a balance between fast synchronization and sufficient stability margin.

3.2. Impact of DLEC bandwidth

Based on the rectifier model described in Fig. 6, the complete closed-loop control block diagram, including both controller and plant dynamics, is constructed as shown in Fig. 11(a). In this diagram, the high-frequency dynamics of the measurement filter $\frac{1}{sT_f+1}$ and control delay $\mathbf{G_{del}(s)}$ are omitted, since their small time constants contribute only non-dominant poles. Given that the inner current control loop's bandwidth is typically designed to be much higher than that of the outer voltage loop, the closed-loop behavior $G_i(s)$ of the inner loop can be accurately approximated by a first-order transfer function, $G_i(s) = \frac{1}{sT_i+1}$. This approximation, along with the cancellation of the internal term $(1.5u_{sd})$ yields the reduced-order form in Fig. 11(b). Moreover, the diagram can be further reduced to the equivalent closed-loop form in Fig. 11(c) because the buck converter power $(P_{dc,i})$ functions as a feedforward disturbance that is directly compensated, and thus does not affect the closed-loop characteristics.

According to the equivalent closed-loop control block diagram in Fig. 11(c), the open-loop and closed-loop dynamics of the DLEC method can be derived as:

$$G_{dlec}^{(op)}(s) = \frac{2k_{p,dlec}s + 2k_{p,dlec}k_{i,dlec}}{C_{dc}s^2(sT_i+1)} \tag{11a}$$

$$G_{dc}^{(cl)}(s) = \frac{2k_{p,dc}s + 2k_{p,dc}k_{i,dc}}{C_{dc}s^2(sT_i+1) + 2k_{p,dc}s + 2k_{p,dc}k_{i,dc}} \tag{11b}$$

where T_i is the reciprocal of the bandwidth in rad/s of the inner current loop; $k_{p,dc}$ and $k_{i,dc}$ are PI controller gains. These parameters can be optimally tuned using the symmetrical optimum method [33], yielding:

$$k_{p,dc} = \frac{1}{T_i}\sqrt{\frac{1-\sin\phi}{1+\sin\phi}}C_{dc},\ k_{i,dc} = \left(\frac{1}{T_i}\sqrt{\frac{1-\sin\phi}{1+\sin\phi}}\right)^3 T_i C_{dc} \tag{12}$$

where ϕ is the desired phase margin for the open-loop transfer function $G_{dlec}^{(op)}(s)$.

From (11)–(12), specifying a target phase margin determines the controller gains $k_{p,dc}$ and $k_{i,dc}$, and thereby sets the DLEC bandwidth $\omega_{bw,dc}$, which enables direct analysis of the bandwidth's impact on system stability. The effect is illustrated in Fig. 12. As the bandwidth increases from 5 Hz to 182 Hz, where the inner current loop bandwidth

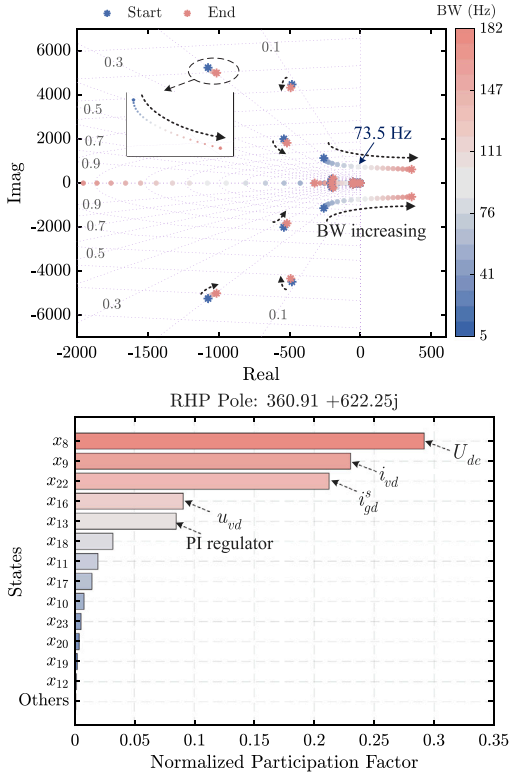

Fig. 12. Impact of the DLEC bandwidth under the inner-loop bandwidth of 300 Hz.

remains fixed at 300 Hz, the dominant poles progressively shift toward the RHP and eventually cause instability at a bandwidth of about 73.5 Hz. These trajectories highlight the need to avoid overly large DLEC bandwidths. This limitation stems from the insufficient bandwidth separation between the two loops. With an outer-loop bandwidth of 73.5 Hz and an inner-loop bandwidth of 300 Hz, the separation ratio is only about 4:1, which does not meet the typical guideline of at least 5:1 [34]. This inadequate separation weakens the timescale decoupling and introduces adverse loop interactions that can lead to instability. Moreover, the participation factor analysis of an unstable RHP pole (360.91 + j622.25) in Fig. 12 indicates that the instability is predominantly associated with the DC-link voltage state (U_{dc}), the d-axis control channel states (i_{vd}, i_{gd}^s, u_{vd}), and the DLEC PI regulator. This evidence confirms that an excessively high DLEC bandwidth establishes

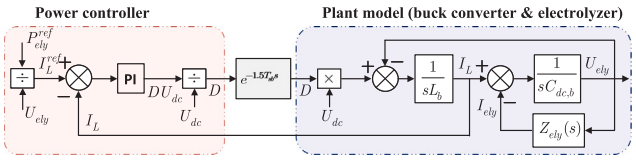

Fig. 13. Control-loop structure of the buck power control.

a destabilizing feedback mechanism between the two loops, driving the system into oscillations.

3.3. Impact of the buck power control bandwidth

According to the buck converter and electrolyzer models described in Fig. 3–Fig. 4, the complete closed-loop control block diagram of the proposed power controller can be drawn, as depicted in Fig. 13. Based on this control diagram and assuming almost constant DC-link voltage U_{dc}, the open-loop dynamic $G^{(op)}_{buck,p}(s)$ of the power control can be derived as:

$$G^{(op)}_{buck,p}(s) = \left(k_{p,b} + \frac{k_{i,b}}{s}\right) \cdot \frac{\overbrace{1 - \frac{1.5T_{sb}s}{2}}^{\approx e^{-1.5T_{sb}s}}}{1 + \frac{1.5T_{sb}s}{2}} \cdot H_b(s) \tag{13a}$$

$$H_b(s) = \frac{C_{dc,b}Z_{ely}(s)s + 1}{L_b C_{dc,b} Z_{ely}(s)s^2 + L_b s + Z_{ely}(s)} \tag{13b}$$

$$Z_{ely}(s) = R_m + \frac{Z_{dl}(s)}{Z_{dl}(s)C_{dl}s + 1} \tag{13c}$$

$$Z_{dl}(s) = R_{act} + \frac{R_{d1}}{R_{d1}C_{d1}s + 1} + \frac{R_{d2}}{R_{d2}C_{d2}s + 1} \tag{13d}$$

where $k_{p,b}$ and $k_{i,b}$ are PI controller gains. The control delay $e^{-1.5T_{sb}s}$ is approximated using a first-order Padé function, where T_{sb} is the reciprocal of the buck converter's switching frequency f_{sb}; $H_b(s)$ represents the plant model dynamic, $\frac{I_L(s)}{D(s)U_{dc}}$; $Z_{ely}(s)$ represents the impedance effect of the electrolyzer stack, i.e. $U_{ely}(s)/I_{ely}(s)$, derived from the stack model in (1)–(2).

The controller gains $k_{p,b}$ and $k_{i,b}$ are tuned to achieve a desired closed-loop bandwidth based on the transfer function, allowing for a direct analysis of the bandwidth's impact on system stability. As shown in Fig. 14, as the bandwidth $\omega_{bw,bu}$ is gradually increased from 1 Hz up to 2840 Hz, most poles initially move leftward, indicating improved tracking and damping performance at low and medium frequencies. However, when the bandwidth exceeds approximately 2684 Hz, one dominant high-frequency eigenvalue is observed to migrate toward the RHP and eventually crosses the imaginary axis (e.g., RHP pole: $2165.61 + j8872.24$).

This instability, revealed by the participation factor analysis in Fig. 14, is intrinsic to the buck converter's control loop. It reveals that the unstable mode is dominated by the duty cycle D, the inductor current I_L, and the PI regulator state, while the contribution of other subsystem states is negligible. The root cause for the instability is the interaction between the high controller gain, required for very high bandwidth, and the inherent control delay ($e^{-1.5T_{sb}s}$), which introduces substantial phase lag at high frequencies.

The results indicate that the buck power control bandwidth should also be strategically selected, presenting a trade-off between fast power regulation and high-frequency stability. Moreover, the localized nature of this instability, as confirmed by the participation factor analysis, has a significant practical implication: the buck converter's control loop can be tuned largely independently, with minimal impact from its dynamic interaction with the front-end rectifier and the grid.

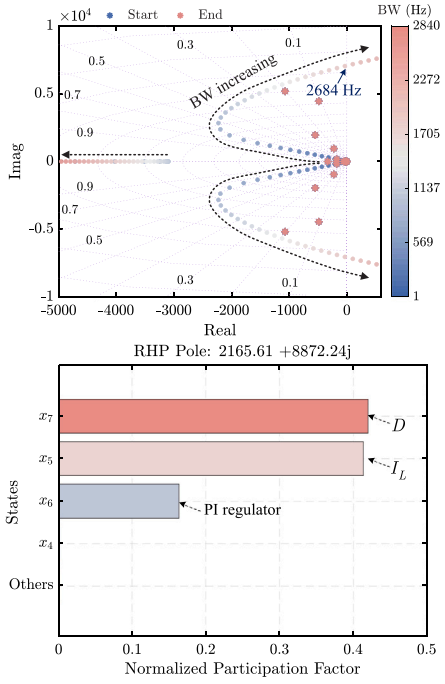

Fig. 14. Impact of the buck converter control bandwidth.

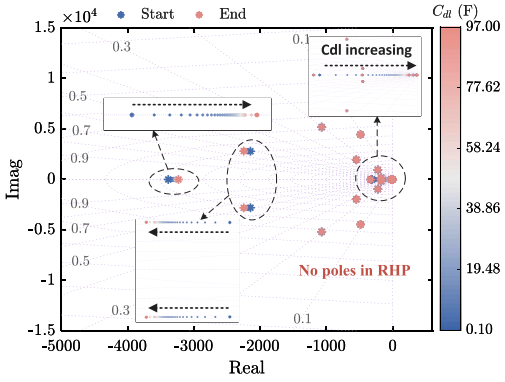

Fig. 15. Impact of C_{dl}.

3.4. Impact of double-layer capacitance effect

Beyond controller parameters, the physical dynamics of the electrolyzer stack itself can also influence system behavior. The stack's voltage dynamics are dominated by the double-layer capacitance effect, characterized by the parameter C_{dl}. This subsection investigates the impact of this key parameter on both system stability and dynamic response, and further clarifies how its influence is coupled with the bandwidth design of the buck converter control.

Fig. 15 shows the eigenvalue trajectories as C_{dl} is varied over a wide range (0.1 F to 97 F), covering its typical estimated values. The root-locus plot indicates that the system is highly robust to this parameter. Although some poles related to the electrolyzer dynamics shift, all eigenvalues remain well within the stable left-half plane. This confirms that the stack dynamics associated with the double-layer capacitance do not pose a direct threat to the small-signal stability of the grid-integrated electrolyzer system.

However, although C_{dl} does not directly compromise small-signal stability, its influence on the system-level power response depends strongly on the buck-control bandwidth. This control dependence can be interpreted quantitatively from (13c)–(13d). In particular, the effect

of the double-layer capacitance on the system response enters through the electrolyzer impedance $Z_{ely}(s)$ in (13c), while the corresponding internal frequency dependence is governed by $Z_{dl}(s)$ in (13d). This indicates that the C_{dl}-related internal stack dynamics are governed not only by C_{dl} itself but also by the frequency-dependent behavior of $Z_{dl}(s)$.

For a simplified first-order RC representation, a single time constant of the form $\tau = RC$ can be directly defined. However, for the third-order electrolyzer model adopted in this work, $Z_{dl}(s)$ is frequency-dependent because it contains two RC diffusion branches with different pole frequencies. As a result, the effective resistance R_{eq} seen by C_{dl} varies with the frequency region of interest.

According to (13d), the pole frequencies of the two RC branches can be expressed as:

$$aaf_{d1} = \frac{1}{2\pi R_{d1}C_{d1}}, \quad f_{d2} = \frac{1}{2\pi R_{d2}C_{d2}} \tag{14}$$

These two pole frequencies define the frequency intervals over which different approximations of R_{eq} become valid. Note that $f_{d1} > f_{d2}$ holds for the studied case, based on the electrolyzer parameter in Table A.1. Accordingly, R_{eq} can be approximately expressed as:

$$aaR_{eq}(\omega) \approx \begin{cases} R_{act} + R_{d1} + R_{d2} & \omega \ll \dfrac{1}{R_{d2}C_{d2}} \\ R_{act} + R_{d1} & \dfrac{1}{R_{d2}C_{d2}} \ll \omega \ll \dfrac{1}{R_{d1}C_{d1}} \\ R_{act} & \omega \gg \dfrac{1}{R_{d1}C_{d1}} \end{cases} \tag{15}$$

This piecewise approximation reflects the different dynamic roles of the two diffusion RC branches in (13d). In the very-low-frequency region, both branches still behave mainly as resistive contributions, so R_{eq} includes R_{act}, R_{d1}, and R_{d2}. In the intermediate-frequency region, the slower R_{d2}–C_{d2} branch has already rolled off, whereas the faster R_{d1}–C_{d1} branch still behaves approximately resistively, so R_{eq} is mainly determined by $R_{act} + R_{d1}$. In the higher-frequency region, both diffusion RC branches have rolled off, and the effective resistance further approaches R_{act}.

Based on this frequency-dependent R_{eq} and the definition of the time constant $\tau = RC$, the third-order electrolyzer model yields a bounded range of effective time constants and the corresponding characteristic frequency region as:

$$\tau_{dl,char} \in \left[R_{act}C_{dl},\ \left(R_{act} + R_{d1} + R_{d2}\right)C_{dl}\right] \tag{16a}$$

$$f_{dl,char} \in \left[\frac{1}{2\pi\left(R_{act} + R_{d1} + R_{d2}\right)C_{dl}},\ \frac{1}{2\pi R_{act}C_{dl}}\right] \tag{16b}$$

Accordingly, the system-level power response becomes weakly sensitive to the C_{dl}-dominated internal stack dynamics when the buck closed-loop bandwidth $f_{bw,bu}$ is designed above the corresponding characteristic frequency region, i.e.,

$$aaf_{bw,bu} > f_{dl,char}^{\max} \tag{17}$$

This provides a practical engineering criterion for weak sensitivity to the C_{dl}-dominated stack dynamics.

In the studied case, based on the electrolyzer parameters in Table A.1, Eq. (14) yields $f_{d2} \approx 1.13$ Hz, $f_{d1} \approx 137.7$ Hz. Eq. (16) yields an effective time-constant range of approximately 0.009–0.022 s, which is equivalently mapped to a characteristic frequency region of about 7.3–17.5 Hz. On this basis, the above theoretical interpretations are verified by the frequency-response results in Figs. 16 and 17.

Fig. 16 compares the frequency response of the buck converter's control loop at a closed-loop bandwidth of 20 Hz. Three electrolyzer models are considered: a static resistive model (Model 1), a first-order RC model (Model 2), and the third-order model used in this work (Model 3). The first two models are commonly used simplifications in the literature [27]. Since 20 Hz already lies above the estimated region for $f_{dl,char}$, the open- and closed-loop responses become nearly

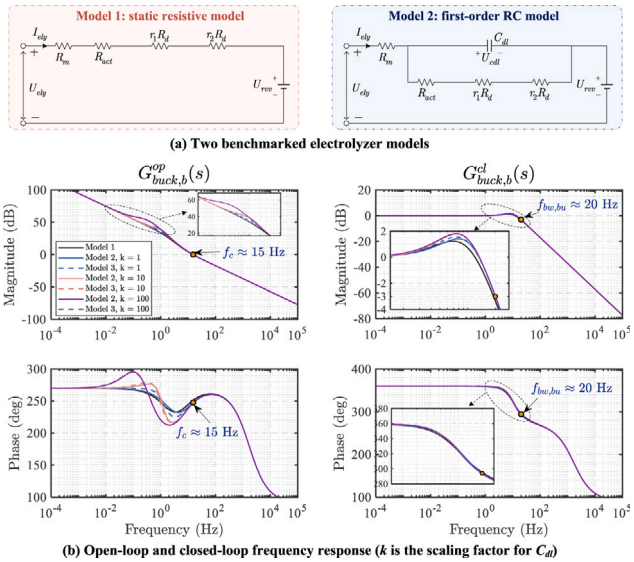

Fig. 16. Frequency response comparison of the buck power control for different electrolyzer models along with various C_{dl}.

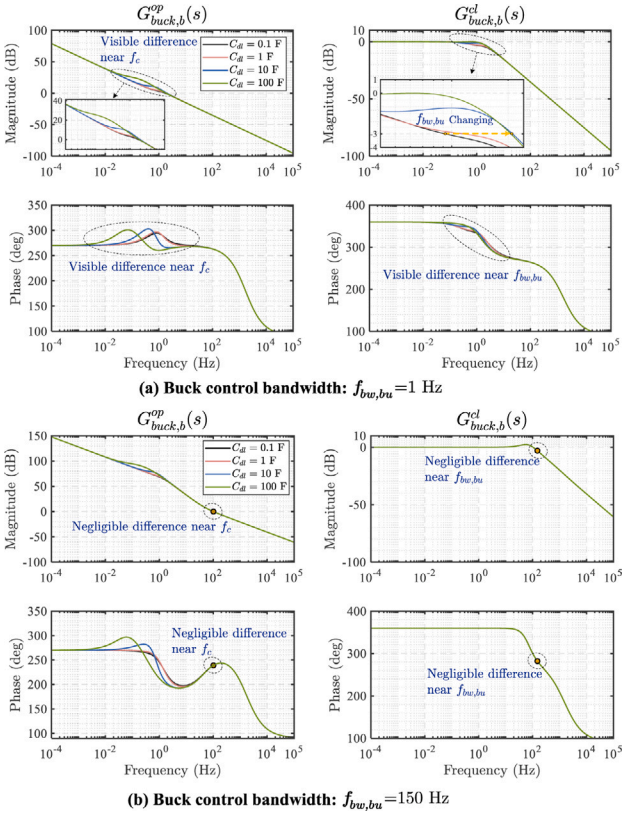

Fig. 17. Sensitivity of the buck power control frequency response to C_{dl} variation under different bandwidth designs.

indistinguishable around the critical bandwidth region, regardless of the model order or the specific value of C_{dl} (scaled by factor k, e.g. $k = 10$ means the $10 \cdot C_{dl}$). Only minor differences still exist at low frequencies.

To further verify this control dependence, the analysis is repeated for two additional bandwidth designs in Fig. 17. Note that, according to (16b), the characteristic frequency region $f_{dl,char}$ is itself dependent on C_{dl}. For the four C_{dl} values considered in Fig. 17, namely 0.1,

Table 1
Quantitative frequency-response difference between the static resistive model (Model 1) and the full model (Model 3) under different buck-control bandwidths.

Buck-control bandwidth (Hz)	Max. open-loop magnitude error near f_c [a] (dB)	Max. open-loop phase error near (deg)	Max. closed-loop magnitude error near $f_{bw,bu}$ [b] (dB)	Max. closed-loop phase error near (deg)
1	2.64	8.82	1.66	7.39
20	0.738	6.75	0.499	1.94
150	0.060	1.78	0.111	0.362

[a] f_c denotes the crossover frequency of the open-loop transfer function.
[b] $f_{bw,bu}$ denotes the −3 dB bandwidth of the closed-loop transfer function.

1, 10, and 100 F, the corresponding characteristic frequency regions are approximately 42.0–101.1 Hz, 4.20–10.1 Hz, 0.420–1.01 Hz, and 0.042–0.101 Hz, respectively. As shown in Fig. 17(a), when the controller is designed for a low bandwidth of 1 Hz, this bandwidth is not sufficiently above the corresponding characteristic frequency regions over the considered C_{dl} range. Consequently, visible differences remain in both magnitude and phase responses around the bandwidth frequency. In contrast, when the controller is designed for a bandwidth of 150 Hz, as shown in Fig. 17(b), this bandwidth is higher than the upper bound of the corresponding characteristic frequency region for all considered C_{dl} values. Accordingly, the corresponding responses become nearly identical.

This finding also helps address the practical uncertainty associated with the double-layer capacitance C_{dl}. In practice, this uncertainty arises because C_{dl} is often unavailable from manufacturers and usually requires case-specific RC fitting, and its identified equivalent value also varies with the operating condition and the identification setting. The proposed analytical framework does not explicitly introduce a stochastic uncertainty model. Instead, it accommodates this uncertainty by identifying the buck-control bandwidth region in which the system-level power response remains sensitive to the C_{dl}-dominated internal dynamics and the region in which such sensitivity becomes weak.

Specifically, for the studied case in this paper, the above analysis yields a clear practical guideline. A buck-control bandwidth of about 20 Hz already acts as a practical lower bound for weak sensitivity to the C_{dl}-dominated internal dynamics, whereas 150 Hz serves as a demonstrated fast-control case with nearly negligible sensitivity. The bandwidth should not be excessively high, since an overly large bandwidth may destabilize the system, as indicated by Fig. 14. Therefore, when the control bandwidth is sufficiently above the C_{dl}-related characteristic frequency region while remaining well below the instability boundary, simplified electrolyzer models can still yield adequate accuracy for system-level power response in grid-interaction studies. This is particularly relevant for applications mainly concerned with external power exchange, such as fast power regulation and grid-frequency support. In contrast, when the control bandwidth is not sufficiently above the characteristic frequency region over the parameter range of interest, the system-level power response remains sensitive to C_{dl} variations. In such cases, or when the study focus is on the internal stack dynamics themselves, more accurate C_{dl} identification and higher-fidelity electrolyzer models become important.

The above observations are further quantified in Table 1, which compares the frequency-response differences between the static resistive model (Model 1) and the full model (Model 3) under representative buck-control bandwidths of 1, 20, and 150 Hz. The reported errors are defined as the maximum absolute magnitude and phase differences within the critical frequency regions, namely $[f_c/3,\ \ 3f_c]$ for the open-loop responses and $[f_{bw,bu}/3,\ \ 3f_{bw,bu}]$ for the closed-loop responses. As the control bandwidth increases from 1 to 150 Hz, both the open- and closed-loop errors decrease markedly, indicating that the discrepancy introduced by the static-model simplification becomes progressively smaller at higher bandwidths. This implies that the simplified static model becomes increasingly acceptable for system-level power-response studies when the control bandwidth is sufficiently high. However, the discrepancies remain non-negligible at low and moderate bandwidths, especially in phase around the critical frequency region. This indicates that the full model remains important not only for providing a more accurate dynamic representation, but also as a higher-fidelity reference when the neglected stack-side dynamics still have a visible influence on the system-level power response.

3.5. Engineering-oriented bandwidth selection and controller-tuning guidelines

The analytical results presented in Sections 3.1–3.4 can be further summarized into engineering-oriented bandwidth selection and controller-tuning guidelines for the studied baseline system. It should be noted that the following numerical values are case-specific, since the exact bandwidth limits vary with the operating point, converter parameters, delay characteristics, and grid conditions. Nevertheless, they illustrate how the proposed analytical framework can be used to derive quantitative and engineering-usable controller-design rules. The resulting guidelines are summarized in Table 2.

For the PLL, the eigenvalue analysis in Section 3.1 shows that increasing the PLL bandwidth drives the dominant poles toward instability, and overly large bandwidth in the few-hundred-Hz region leads to oscillatory instability. Therefore, for the studied case, the PLL bandwidth is recommended to be kept in a conservative low-tens-of-Hz range (e.g., about 10–50 Hz), rather than being pushed into the several-hundred-Hz region.

For the rectifier DLEC, the results in Section 3.2 show that, with the inner current-loop bandwidth fixed at 300 Hz, instability occurs at about 73.5 Hz. This confirms the practical engineering requirement that at least a 5:1 bandwidth separation should be maintained between the outer and inner loops. Accordingly, for the present case, a practical recommendation is to keep the DLEC bandwidth below about 60 Hz.

For the buck power control, the combined eigenvalue and frequency-response analyses in Sections 3.3 and 3.4 reveal a dual-sided design requirement. On the one hand, the control bandwidth should be sufficiently above the low-frequency region where the system power response remains sensitive to the electrolyzer double-layer capacitance C_{dl}. On the other hand, it should remain well below the control delay-induced instability threshold of about 2684 Hz. In the studied case, 20 Hz can be regarded as a practical lower bound for achieving weak sensitivity to the C_{dl}-dominated electrolyzer stack dynamics, whereas 150 Hz serves as a demonstrated fast-control case that still remains far from the high-frequency instability region. Therefore, a conservative engineering range of about 20–150 Hz is recommended for the buck power control in the present baseline system.

In addition, the proposed framework provides engineering-usable tuning principles. Specifically, the PLL gains can be directly determined from the target natural frequency (which is proportional to the bandwidth, as stated before) and damping ratio through (10); the DLEC gains are designed via the symmetrical optimum framework in (11)–(12), in which the selected phase margin implicitly determines the achieved outer-loop bandwidth; and the buck-controller gains are selected through the transfer-function-based design in (13) to achieve a desired closed-loop bandwidth while respecting the stability constraints revealed by the eigenvalue analysis.

Table 2
Engineering-oriented bandwidth selection and controller-tuning guidelines for the studied case.

Control loop	Quantitative analytical observation	Bandwidth selection guideline	Tuning principle
PLL	Increasing PLL bandwidth drives dominant poles toward instability; oscillatory instability appears when the bandwidth enters the few-hundred-Hz region.	Keep the PLL bandwidth in a conservative low-tens-of-Hz range (e.g., about 10–50 Hz).	Determine $k_{p,\mathrm{pll}}$ and $k_{i,\mathrm{pll}}$ from (10) using the target natural frequency and damping ratio.
DLEC	With the inner current-loop bandwidth fixed at 300 Hz, instability occurs at about 73.5 Hz; at least a 5:1 outer/inner bandwidth separation is required.	Keep the DLEC bandwidth below about 60 Hz.	Select $k_{p,\mathrm{dc}}$ and $k_{i,\mathrm{dc}}$ via the symmetrical optimum design in (11)–(12); the chosen phase margin implicitly sets the achieved outer-loop bandwidth.
Buck power control	The power response remains sensitive to C_{dl} at low frequency; weak sensitivity is achieved above about 20 Hz; the control delay-induced instability threshold is about 2684 Hz.	Conservative engineering range: about 20–150 Hz.	Select $k_{p,b}$ and $k_{i,b}$ through the transfer-function-based design in (13) to achieve the desired closed-loop bandwidth while staying well below the instability region.

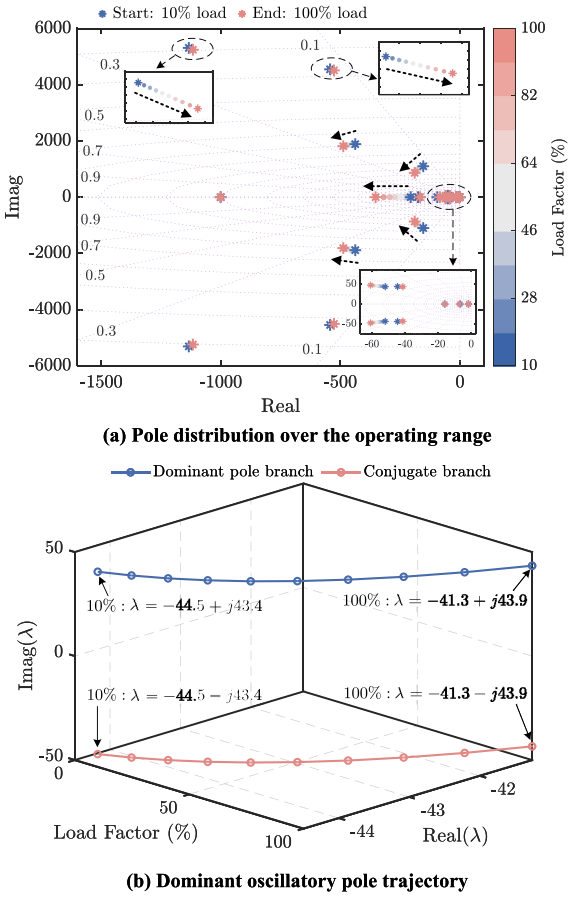

Fig. 18. Small-signal stability over the full electrolyzer loading range: (a) pole distribution over the operating range; (b) 3D trajectory of the dominant oscillatory pole pair as the load factor varies from 10% to 100%.

3.6. Small-signal stability over electrolyzer loading range

The eigenvalue-based analyses presented above are mainly carried out around the nominal operating point. To further examine this operating-point dependence, a supplementary operating-point sweep is carried out over the full electrolyzer loading range from 10% to 100%. For each loading level, the nonlinear analytical model is first brought to the corresponding steady operating point, and the system is then linearized around that operating point. Based on these operating-point-dependent linearizations, Fig. 18 presents the pole distribution over the full operating range and the 3D trajectory of the dominant oscillatory pole pair.

As shown in Fig. 18(a), all poles remain in the stable left-half plane over the investigated loading range, indicating that no loss of small-signal stability occurs between low-load and full-load conditions for the studied case. Furthermore, the smooth trajectories in Fig. 18(b) show that the dominant oscillatory mode does not undergo abrupt switching as the operating point changes. The dominant conjugate pole pair exhibits only a slight movement, shifting from approximately $-44.5 \pm j43.4$ at 10% load to $-41.3 \pm j43.9$ at 100% load.

These results indicate that, although the PEM stack is nonlinear, the operating-point dependence of the small-signal stability is relatively weak over the full loading range for the studied system configuration. Therefore, the nominal-point eigenvalue conclusions presented in Section 3 remain broadly representative over the examined full loading range.

4. Case studies

To demonstrate the theoretical stability findings based on eigenvalue analysis presented in Section 3, a detailed EMT model of the grid-integrated electrolyzer system (Fig. 1) is developed in PSCAD/EMTDC. All system and control parameters, listed in Appendix (Table A.1), are kept identical to those used in the previous theoretical analysis to ensure one-to-one comparison. The following subsections present the time-domain demonstration of the key dynamic behaviors and stability boundaries revealed by the eigenvalue analysis.

4.1. Demonstration of PLL bandwidth impact

The previous eigenvalue analysis indicates that an excessively high PLL bandwidth would destabilize the system through high-frequency oscillations. This is verified in the time-domain results shown in Fig. 19, where the PLL bandwidth is stepped from a stable 10 Hz to an unstable 500 Hz at $t = 5$ s. Immediately following the change, the system becomes unstable. The primary evidence of this instability is the high-frequency oscillation in the PLL's output frequency, which occurs at approximately 690 Hz, providing a close quantitative match to the unstable mode (governed by the RPH pole) presented in Fig. 10. This PLL-driven instability propagates throughout the system, leading to severe distortions in the grid-side current and PCC voltage waveforms, both of which also deviate from their nominal values. It also induces oscillations in the DC-link voltage, as well as in the electrolyzer's active and reactive power exchanged with the grid. These results clearly demonstrate that an excessively large PLL bandwidth can destabilize the entire system, aligning with the theoretical stability analysis.

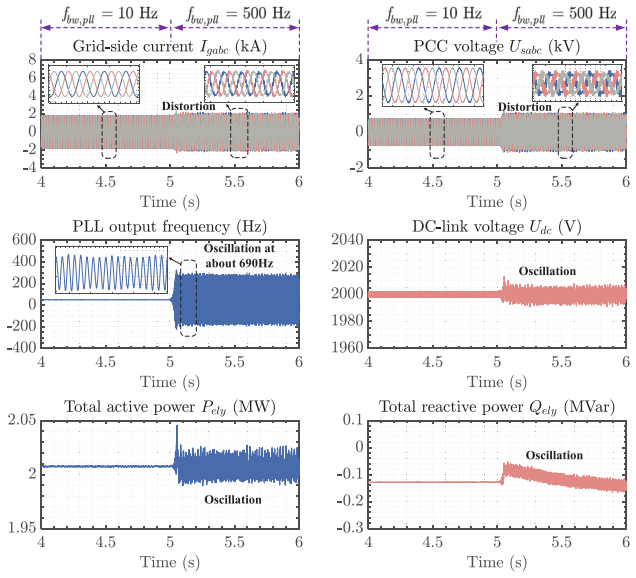

Fig. 19. Electrolyzer system response when the PLL bandwidth changes from 10 Hz to 500 Hz at $t = 5$ s.

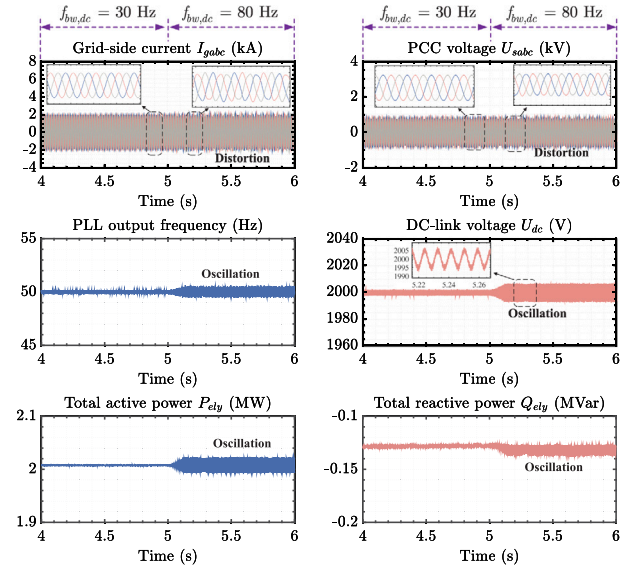

Fig. 20. Electrolyzer system response when the DLEC bandwidth changes from 30 Hz to 80 Hz at $t = 5$ s.

4.2. Demonstration of DLEC bandwidth impact

Regarding the DLEC for the rectifier, the eigenvalue analysis indicates that the DLEC bandwidth is limited by the inner current loop's bandwidth, predicting that an excessively high bandwidth will cause an instability. This behavior is demonstrated in Fig. 20, where the DLEC bandwidth is stepped from a stable 30 Hz to a predicted unstable value of 80 Hz at $t = 5$ s. Following the change, the system enters a state of sustained oscillation. This instability is primarily revealed by the persistent oscillation observed in the DC-link voltage, PLL output frequency, and the active/reactive power. This underlying instability then propagates to the AC side, causing severe distortion in the grid-side current and PCC voltage waveforms, thus confirming the theoretical findings.

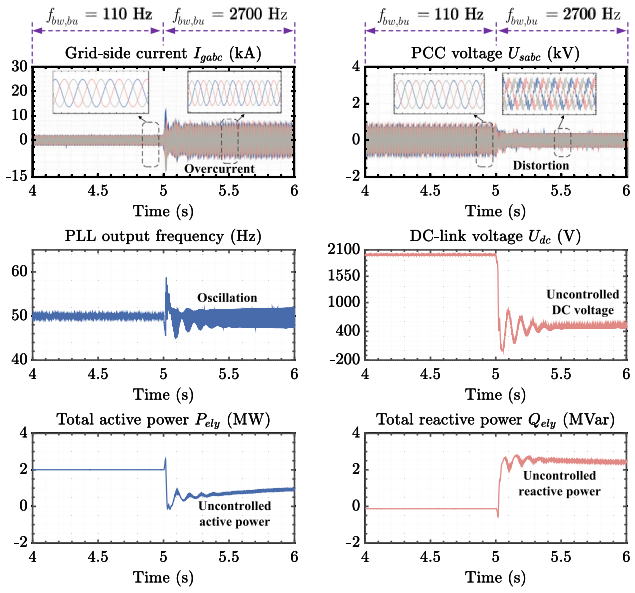

Fig. 21. Electrolyzer system response when the buck power control bandwidth changes from 110 Hz to 2700 Hz at $t = 5$ s.

4.3. Demonstration of buck converter bandwidth impact

The previous stability analysis predicted that the buck converter's control loop would become unstable at a very high bandwidth due to internal dynamics and control delays. This is demonstrated in Fig. 21, which shows the system's response to a step change in the buck control bandwidth from a stable 110 Hz to an unstable 2700 Hz at $t = 5$ s. The system response is an immediate and severe failure. The DC-link voltage and active/reactive power become completely uncontrolled, and PLL output exhibits obvious oscillations. Simultaneously, the PCC voltage deviates far from its nominal level and, along with the grid-side current, becomes severely distorted, with the current also exhibiting large overcurrent spikes. This time-domain result perfectly matches the theoretical prediction that the buck converter's instability occurs at an overlarge bandwidth.

4.4. Demonstration of double-layer capacitance impact

An appropriately designed control bandwidth makes the system's power response robust to the electrolyzer stack's capacitive dynamics, which is indicated by the aforementioned eigenvalue analysis. This finding is also demonstrated via the time-domain simulation. The test is conducted by applying a power step change, with the buck converter's control bandwidth set to a moderate 20 Hz. Fig. 22(a) shows the system response for different values of the double-layer capacitance C_{dl}. While the electrolyzer's internal voltage (U_{ely}) exhibits a significantly slower transient with a larger C_{dl}, the critical system-level active power response (P_{ely}) is nearly identical across all cases. This directly confirms the previous Bode-response analysis: at a 20 Hz bandwidth, the closed-loop power response is already weakly sensitive to the stack voltage dynamics governed by C_{dl}. This principle is further reinforced in Fig. 22(b), which shows that using different electrolyzer model orders (full-order vs. reduced-order) also yields nearly indistinguishable external power responses, despite variations in the internal voltage behavior.

These results demonstrate that for studies focused on the system's external power exchange with the grid (e.g., grid frequency support), a moderately high control bandwidth can render the power response largely insensitive to the complex and often uncertain electrolyzer stack dynamics governed by the double-layer capacitance effect. Given that

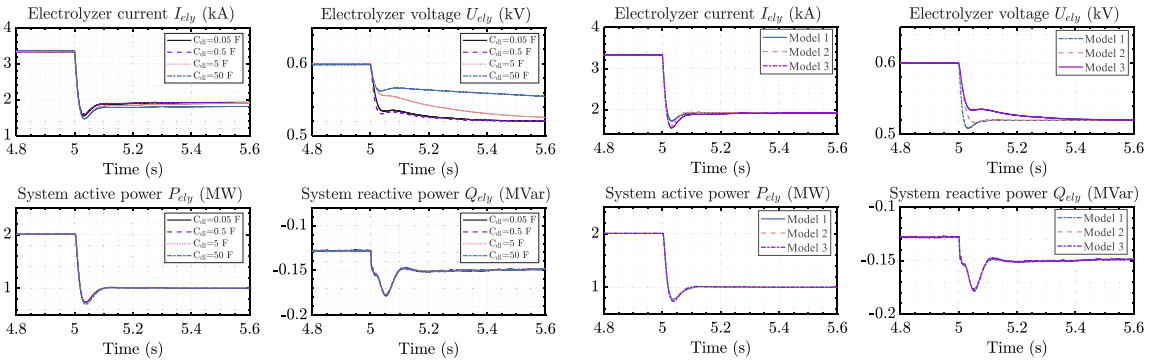

(a) System response under power step change when different C_{dl} (b) System response under power step change using different stack models

Fig. 22. Electrolyzer system response under different C_{dl} and stack models.

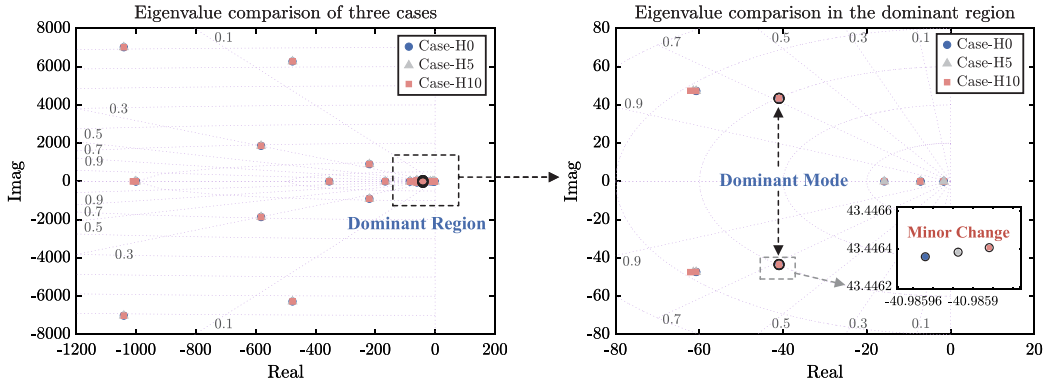

Fig. 23. System eigenvalue comparison of three cases: Case-H0, Case-H5, Case-H10.

accurately identifying such internal dynamics, particularly the double-layer capacitance C_{dl}, is often difficult since these parameters are rarely offered by manufacturers and require case-specific RC model fitting, this finding provides strong practical justification for a model reduction strategy. It enables the use of simpler, or even static, electrolyzer models in such applications, thereby reducing modeling complexity while ensuring sufficient accuracy for the power dynamic assessment.

4.5. Effect of module parameter inconsistency

The scalability formulation introduced in Section 2.6 is established under the simplifying assumption of homogeneous modules and units. In practice, however, parallel electrolyzer modules may exhibit parameter dispersion due to manufacturing tolerances or different aging conditions. To examine whether such inconsistency may alter the dominant stability characteristics identified in Section 3, an auxiliary heterogeneous-case study is carried out here.

Specifically, a two-parallel-module case is considered, i.e., $N_{mo} = 2$ and $N_{unit} = 1$, where two electrolyzer modules are connected through a shared rectifier/DC-link interface, consistent with the scalable configuration shown in Fig. 9. Module 1 retains the baseline parameters in Table A.1, while Module 2 is assigned deviations in the key stack electrochemical resistive and capacitive parameters to emulate practical mismatch. Three representative cases are examined: Case-H0 (0% mismatch), Case-H5 (5% mismatch), and Case-H10 (10% mismatch). In addition, a mismatch sweep from 0% to 10% is performed to reveal the sensitivity trend more clearly.

Fig. 23 compares the eigenvalue distributions of Case-H0, Case-H5, and Case-H10. It can be observed that the eigenvalue spectra remain very close to each other, and even in the zoomed dominant region only negligible modal shifts are introduced by module mismatch. No distinct new low-damped oscillatory mode is observed within the investigated mismatch range.

To further quantify the influence of parameter inconsistency, Fig. 24(a) presents the variations of two damping-related indices as the mismatch level increases from 0% to 10%: the minimum damping ratio among all oscillatory modes and the damping ratio of the most mismatch-sensitive oscillatory mode (i.e., the mode showing the largest pole shift as the module-mismatch level increases). Both indices remain nearly unchanged over the entire sweep, with maximum relative deviations of only 0.00003696% and 0.00608%, respectively. This indicates that mild module-to-module parameter inconsistency has a negligible effect on the system's dominant damping characteristics in the investigated range.

The physical nature of the mismatch-sensitive mode is further examined through the participation-factor analysis in Fig. 24(b) for Case-H10. The corresponding mode is located at $\lambda = -62.19 + 47.43j$ with a damping ratio of $\zeta = 0.7952$, indicating that it remains well damped. Its dominant participation is associated mainly with the local buck-converter and stack-side states, including the inductor current I_L, the buck PI regulator, the internal stack voltages U_{cdl} and U_{d2}, as well as the buck-control delay state. Therefore, the mode most affected by the introduced mismatch is still essentially a local buck, stack, and control mode, rather than a newly emerged poorly damped inter-module oscillatory mode.

Overall, these results show that mild practical module parameter inconsistency, within the investigated 0%–10% mismatch range, introduces only negligible modal shifts and does not fundamentally alter the dominant stability conclusions derived for the baseline system. This also supports the use of the homogeneous scalability assumption in Section 2.6 for system-level studies within such a practically mild mismatch range.

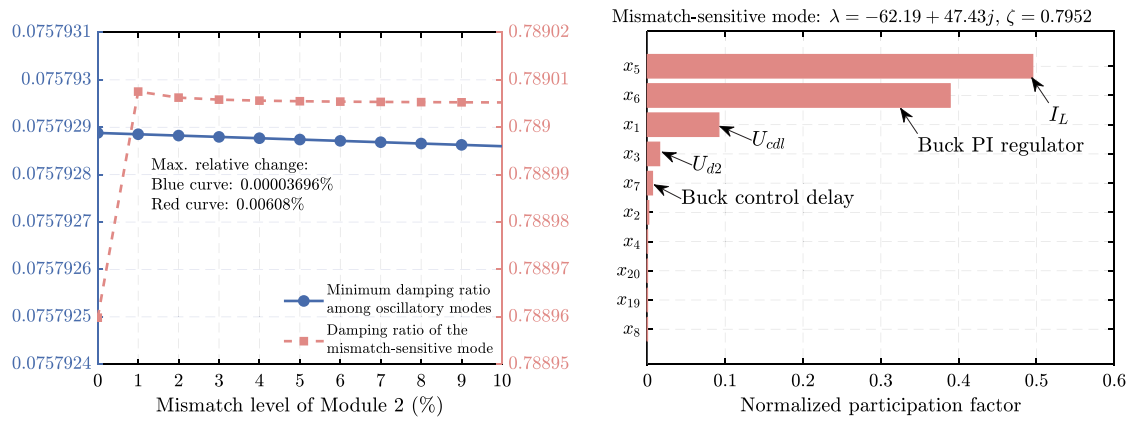

(a) Sensitivity of damping characteristics to module mismatch

(b) Participation factors of the most mismatch-shifted oscillatory mode in Case-H10

Fig. 24. Sensitivity and participation-factor analysis of the mismatch-affected oscillatory mode.

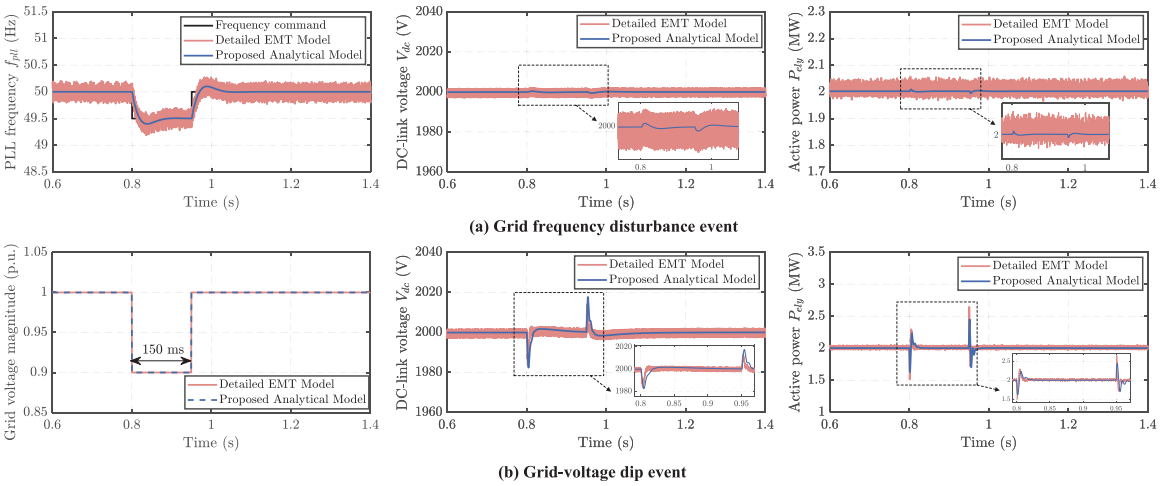

(a) Grid frequency disturbance event

(b) Grid-voltage dip event

Fig. 25. Time-domain response comparisons between the proposed analytical model and the detailed EMT model under (a) a grid frequency disturbance event and (b) a grid-voltage dip event.

4.6. Demonstration of the proposed analytical model under representative grid events

To further verify the predictive capability of the proposed analytical model beyond eigenvalue-based analysis, additional time-domain demonstrations are carried out under two representative grid events, namely a grid frequency disturbance and a grid-voltage dip. Specifically, the dynamic responses of the proposed analytical model are compared against those of a detailed EMT model under: 1) a frequency disturbance event of 50 → 49.5 → 50 Hz with a duration of 150 ms; and 2) a grid-voltage dip event of 1.0 → 0.9 → 1.0 p.u. with a duration of 150 ms.

Fig. 25 presents the corresponding comparisons. For the grid frequency disturbance event, representative and key dynamic response indices, including the PLL frequency f_{pll}, DC-link voltage V_{dc}, and electrolyzer active power P_{ely}, are compared. It can be observed that the proposed analytical model shows good agreement with the detailed EMT model in terms of disturbance timing, dominant excursion pattern, and recovery behavior. The visible high-frequency ripple in the EMT responses is expected, because the detailed EMT model includes explicit converter switching, whereas the proposed analytical model adopts averaged converter dynamics. Therefore, slight ripple-level discrepancies do not affect the good agreement in the dominant transient envelope, event timing, and recovery behavior. As further quantified in Table 3, the maximum relative errors of the selected dominant response indices are only 0.264% and 0.214% for f_{pll}, 0.0318% and 0.00397% for V_{dc}, and 0.872% and 1.486% for P_{ely} during the disturbance stage and recovery stage, respectively.

For the grid-voltage dip event, the imposed grid-voltage profile together with the corresponding representative and key dynamic responses, namely the DC-link voltage and electrolyzer active power, are further compared, as shown in Fig. 25(b). The proposed analytical model reproduces the detailed EMT results with very close agreement for the DC-link voltage response and good agreement for the active-power response. The maximum relative errors of the selected dominant response indices are 0.153% and 0.278% for V_{dc}, and 5.639% and 5.922% for P_{ely}, during the disturbance stage and recovery stage, respectively. Although the active-power response under the grid-voltage dip event shows slight deviations in the dominant transient peak, the main dynamic trend, the event timing, and the recovery process are still captured well by the proposed model.

Therefore, the above results provide further evidence that the proposed analytical model can effectively reproduce the key transient behaviors of the detailed EMT model under representative grid events, while maintaining much lower modeling complexity. They explicitly confirm the practical applicability of the proposed analytical model under the typical grid disturbances studied.

Table 3
Maximum relative errors of selected dominant response indices between the proposed analytical model and the detailed EMT model.

Grid frequency disturbance event			Grid-voltage dip event		
Index	Disturbance stage	Recovery stage	Index	Disturbance stage	Recovery stage
f_{pll}	0.264%	0.214%	V_{dc}	0.153%	0.278%
V_{dc}	0.0318%	0.00397%			
P_{ely}	0.872%	1.486%	P_{ely}	5.639%	5.922%

5. Conclusion

This paper presents a holistic analytical modeling framework for grid-integrated electrolyzer systems interfaced through a two-stage converter topology consisting of an active front-end rectifier and a buck converter. By explicitly integrating the electrolyzer stack, the multi-loop converter controls, and the grid-side dynamics into a unified analytical model, the proposed framework enables systematic stability assessment and quantitative interpretation of the internal dynamic interactions in grid-integrated electrolyzer systems. The key findings are summarized as follows:

(1) The system stability is strongly affected by control-bandwidth design, although the underlying mechanisms differ among control loops. Based on the quantified impact of control-parameter sensitivities on system stability, engineering-oriented bandwidth selection and controller-tuning guidelines are established. Specifically, for the studied 2 MW electrolyzer case, the PLL should be kept within about 10–50 Hz, the rectifier DLEC bandwidth below about 60 Hz, and the buck power-control bandwidth within about 20–150 Hz. Bandwidths largely exceeding these ranges will trigger oscillatory instabilities.

(2) The double-layer capacitance does not directly threaten the system's small-signal stability, but its effect on the system-level power response is bandwidth-dependent. For the 2 MW electrolyzer case, the capacitance-dominated internal stack dynamics are associated with a characteristic frequency region of about 7.3–17.5 Hz. Accordingly, a buck-control bandwidth of about 20 Hz already acts as a practical lower bound for weak sensitivity to these slow stack dynamics, whereas 150 Hz yields nearly negligible sensitivity. This provides a quantitative basis for model-fidelity selection in system-level grid-interaction studies.

(3) The nominal-point small-signal conclusions remain representative over the full load range and under mild parameter inconsistency between electrolyzer modules. Over the full loading range from 10% to 100%, all poles remain in the stable left-half plane, and the dominant pole pair moves only slightly, from approximately $-44.5 \pm j43.4$ to $-41.3 \pm j43.9$. In addition, under 0%–10% module mismatch, the damping-ratio deviations remain negligible, below 0.01%, and no new poorly damped inter-module oscillatory mode emerges.

(4) The proposed analytical model shows good predictive capability under representative grid disturbances. Under a 1% grid-frequency drop, the maximum relative errors of the representative response indices between the proposed analytical model and the detailed EMT model are only 0.264%–1.486%; under a 10% grid-voltage dip, the corresponding errors are 0.153%–5.922%. These results confirm good agreement between the proposed analytical model and the detailed EMT model under practically relevant grid disturbances.

(5) Compared with a simplified electrolyzer model, the proposed holistic model not only provides a more accurate dynamic representation, but also serves as a high-fidelity reference for judging when model reduction remains acceptable. The quantitative comparison between the two models reveals that, at a low buck-control bandwidth of 1 Hz, the discrepancies remain non-negligible, reaching 2.64 dB and 8.82° in the open-loop critical region, whereas at 150 Hz they become very small (e.g., 0.060 dB and 1.78° in open loop). This clarifies the added value of the proposed model and the applicability boundary of simplified electrolyzer models for system-level studies.

Future work will extend the proposed analytical modeling framework toward large-scale renewable-to-hydrogen plants, while also pursuing experimental validation of complete grid-integrated electrolyzer systems. It will focus on the stability of interconnected systems comprising renewable generation units and multiple electrolyzers, including those operating under advanced grid-forming control strategies. Particular attention will be devoted to coordinated parameter design and optimization across all interfaced converters. These efforts will further support the practical applicability of the proposed framework, while mitigating adverse oscillatory phenomena and enhancing the overall robustness of renewable-powered hydrogen production systems.

CRediT authorship contribution statement

Chunjun Huang: Writing – original draft, Visualization, Validation, Methodology, Investigation, Formal analysis, Data curation, Conceptualization. **José Luis Rueda Torres:** Writing – review & editing, Supervision, Project administration, Methodology, Funding acquisition, Conceptualization. **Nakul Narayanan Kuruveettil:** Writing – review & editing, Methodology, Investigation, Formal analysis. **Xin Jin:** Writing – review & editing, Visualization, Investigation, Formal analysis.

Declaration of competing interest

The authors declare that they have no known competing financial interests or personal relationships that could have appeared to influence the work reported in this paper.

Acknowledgments

This work is supported by received funding from TenneT TSO B.V. within the FUTURESYSTEM research project ‘‘Adaptive fast active power control for stabilization of multi-converter dynamics in offshore electrical energy hydrogen hubs”. It reflects only the authors' views, and the aforesaid organization is not responsible for any use that may be made of the paper's content.

Appendix A. Supplementary data

Supplementary material related to this article can be found online at https://doi.org/10.1016/j.ijhydene.2026.155391.

References

[1] Ma N, Zhao W, Wang W, Li X, Zhou H. Large scale of green hydrogen storage: Opportunities and challenges. Int J Hydrog Energy 2024;50:379–96. http://dx.doi.org/10.1016/j.ijhydene.2023.09.021.

[2] Grigoriev SA, Fateev VN, Bessarabov DG, Millet P. Current status, research trends, and challenges in water electrolysis science and technology. Int J Hydrog Energy 2020;45(49):26036–58. http://dx.doi.org/10.1016/j.ijhydene.2020.03.109.

[3] Sayed-Ahmed H, Toldy ÁI, Santasalo-Aarnio A. Dynamic operation of proton exchange membrane electrolyzers—Critical review. Renew Sustain Energy Rev 2024;189:113883. http://dx.doi.org/10.1016/j.rser.2023.113883.

[4] Majumdar A, Haas M, Elliot I, Nazari S. Control and control-oriented modeling of PEM water electrolyzers: A review. Int J Hydrog Energy 2023;48(79):30621–41. http://dx.doi.org/10.1016/j.ijhydene.2023.04.204.

[5] Rauls E, Hehemann M, Scheepers F, Müller M, Peters R, Stolten D. System dynamics of polymer electrolyte membrane water electrolyzers and impact of renewable energy sources on systems design. Int J Hydrog Energy 2024;65:83–94. http://dx.doi.org/10.1016/j.ijhydene.2024.03.302.

[6] El Kattel MB, Praça PP, Mayer R, Lucio Berrehil el Kattel CdC, Bascope RPT, Antunes FLM, de Jesus Cardoso Filho B. Overview of main electrolyzer technologies and power electronic converter topologies for enabling hydrogen production through water electrolysis. Int J Circuit Theory Appl 2025;53(6):3684–718. http://dx.doi.org/10.1002/cta.4277.

[7] Sanchez L, Reigosa D, Bilbao A, Pena-Gonzalez I, Briz F. Comparative analysis of power converter topologies for hydrogen electrolyzers. IEEE J Emerg Sel Top Power Electron 2024;12(5):4325–41. http://dx.doi.org/10.1109/JESTPE.2024.3417258.

[8] Wang B, Xin D, Fu Q, Zhang C. A control-oriented comprehensive model of PEM electrolyzer considering double-layer capacitance. Int J Hydrog Energy 2024;93:866–77. http://dx.doi.org/10.1016/j.ijhydene.2024.11.046.

[9] Sakas G, Rentschler P, Kosonen A, Holtappels P, Ruuskanen V, Kauranen P, Ahola J, Dittmeyer R. Dynamic mass and energy balance model of a 50 kw proton exchange membrane electrolyzer system. Appl Energy 2025;382:125199. http://dx.doi.org/10.1016/j.apenergy.2024.125199.

[10] Huang C, Zong Y, You S, Træ holt C. Analytical modeling and control of grid-scale alkaline electrolyzer plant for frequency support in wind-dominated electricity-hydrogen systems. IEEE Trans Sustain Energy 2022;14(1):217–32. http://dx.doi.org/10.1109/TSTE.2022.3208361.

[11] Dozein MG, Jalali A, Mancarella P. Fast frequency response from utility-scale hydrogen electrolyzers. IEEE Trans Sustain Energy 2021;12(3):1707–17. http://dx.doi.org/10.1109/TSTE.2021.3063245.

[12] Dozein MG, De Corato AM, Mancarella P. Virtual inertia response and frequency control ancillary services from hydrogen electrolyzers. IEEE Trans Power Syst 2022;38(3):2447–59. http://dx.doi.org/10.1109/TPWRS.2022.3181853.

[13] Kumar RK, Samuel P. Designing a hydrogen generation system through PEM water electrolysis with the capability to adjust fast fluctuations in photovoltaic power. Int J Hydrog Energy 2024;82:1–10. http://dx.doi.org/10.1016/j.ijhydene.2024.07.376.

[14] Wang B, Zhaoxiang B. Hydrogen energy storage: Mitigating variability in wind and solar power for grid stability in Australia. Int J Hydrog Energy 2025;97:1249–60. http://dx.doi.org/10.1016/j.ijhydene.2024.11.491.

[15] Cheng X, Lin J, Liu F, Qiu Y, Song Y, Li J, Wu S. A coordinated frequency regulation and bidding method for wind-electrolysis joint systems participating within ancillary services markets. IEEE Trans Sustain Energy 2022;14(3):1370–84. http://dx.doi.org/10.1109/TSTE.2022.3233062.

[16] Zheng Y, Huang C, You S, Zong Y. Economic evaluation of a power-to-hydrogen system providing frequency regulation reserves: a case study of Denmark. Int J Hydrog Energy 2023;48(67):26046–57. http://dx.doi.org/10.1016/j.ijhydene.2023.03.253.

[17] Wang Y, Wang X, Chen Z, Blaabjerg F. Small-signal stability analysis of inverter-fed power systems using component connection method. IEEE Trans Smart Grid 2017;9(5):5301–10. http://dx.doi.org/10.1109/TSG.2017.2686841.

[18] Yang D, Wang X. Unified modular state-space modeling of grid-connected voltage-source converters. IEEE Trans Power Electron 2020;35(9):9700–15. http://dx.doi.org/10.1109/TPEL.2020.2965941.

[19] Sun J. Impedance-based stability criterion for grid-connected inverters. IEEE Trans Power Electron 2011;26(11):3075–8. http://dx.doi.org/10.1109/TPEL.2011.2136439.

[20] Yang D, Sun Y. SISO impedance-based stability analysis for system-level small-signal stability assessment of large-scale power electronics-dominated power systems. IEEE Trans Sustain Energy 2021;13(1):537–50. http://dx.doi.org/10.1109/TSTE.2021.3119207.

[21] Fang W, Teng Y, Zhang S, Kong H, Wang H, Guo X. Impedance modeling and stability analysis of electrolysis system for hydrogen production under weak grid. Fuel 2024;374:132403. http://dx.doi.org/10.1016/j.fuel.2024.132403.

[22] Mu H, Yang D, Sun Y, Larumbe LB. Dynamic power tracking performance and small signal stability analysis of integrated wind-to-hydrogen system. IEEE Trans Sustain Energy 2024;15(4):2444–56. http://dx.doi.org/10.1109/TSTE.2024.3422133.

[23] Hegge A, Avdiaj E, Beerten J, Kircheis J. Small signal modeling of electrolyzers and their interaction with power system dynamics. In: 2025 IEEE kiel powerTech. IEEE; 2025, p. 1–7. http://dx.doi.org/10.1109/PowerTech59965.2025.11180245.

[24] Agredano-Torres M, Zhang M, Söder L, Xu Q. Decentralized dynamic power sharing control for frequency regulation using hybrid hydrogen electrolyzer systems. IEEE Trans Sustain Energy 2024;15(3):1847–58. http://dx.doi.org/10.1109/TSTE.2024.3381491.

[25] Yodwong B, Guilbert D, Phattanasak M, Kaewmanee W, Hinaje M, Vitale G. Proton exchange membrane electrolyzer modeling for power electronics control: A short review, C 6 (2). 2020, p. 29. http://dx.doi.org/10.3390/c6020029.

[26] Hossain MB, Islam MR, Muttaqi KM, Sutanto D, Agalgaonkar AP. Dynamic electrical circuit modeling of a proton exchange membrane electrolyzer for frequency stability, resiliency, and sensitivity analysis in a power grid. IEEE Trans Ind Appl 2023;59(6):7271–81. http://dx.doi.org/10.1109/TIA.2023.3297985.

[27] Ratib MK, Muttaqi KM, Islam MR, Sutanto D, Agalgaonkar AP. Electrical circuit modeling of proton exchange membrane electrolyzer: The state-of-the-art, current challenges, and recommendations. Int J Hydrog Energy 2024;49:625–45. http://dx.doi.org/10.1016/j.ijhydene.2023.08.319.

[28] Martinson CA, Van Schoor G, Uren KR, Bessarabov D. Characterisation of a PEM electrolyser using the current interrupt method. Int J Hydrog Energy 2014;39(36). http://dx.doi.org/10.1016/j.ijhydene.2014.09.153.

[29] Erickson RW, Maksimovic D. Fundamentals of power electronics. 2nd ed.. New York, NY: Springer; 2001, http://dx.doi.org/10.1007/b100747.

[30] Zarei SF, Mokhtari H, Ghasemi MA, Peyghami S, Davari P, Blaabjerg F. Control of grid-following inverters under unbalanced grid conditions. IEEE Trans Energy Convers 2019;35(1):184–92. http://dx.doi.org/10.1109/TEC.2019.2945699.

[31] Guo J, Chen Y, Wang L, Wu W, Wang X, Shuai Z, Guerrero JM. Impedance analysis and stabilization of virtual synchronous generators with different DC-link voltage controllers under weak grid. IEEE Trans Power Electron 2021;36(10):11397–408. http://dx.doi.org/10.1109/TPEL.2021.3070038.

[32] Wen B, Boroyevich D, Burgos R, Mattavelli P, Shen Z. Analysis of DQ small-signal impedance of grid-tied inverters. IEEE Trans Power Electron 2015;31(1):675–87. http://dx.doi.org/10.1109/TPEL.2015.2398192.

[33] D'Arco S, Suul JA, Fosso OB. Automatic tuning of cascaded controllers for power converters using eigenvalue parametric sensitivities. IEEE Trans Ind Appl 2014;51(2):1743–53. http://dx.doi.org/10.1109/TIA.2014.2354732.

[34] Zarei SF, Mokhtari H, Ghasemi MA, Peyghami S, Davari P, Blaabjerg F. DC-link loop bandwidth selection strategy for grid-connected inverters considering power quality requirements. Int J Electr Power Energy Syst 2020;119:105879. http://dx.doi.org/10.1016/j.ijepes.2020.105879.